

Transformation toughness induced by surface tension of the crack-tip process zone interface: A field-theoretical approach

Alexei Boulbitch^{1,*} and Alexander L. Korzhenevskii²

¹Zum Waldeskühl 12, 54296 Igel, Germany

²Institute for Problems of Mechanical Engineering, Russian Academy of Sciences, Bol'shoi Prospect V.O. 61, 199178 Saint Petersburg, Russia

 (Received 5 October 2020; revised 26 December 2020; accepted 11 January 2021; published 5 February 2021)

We study a crystal with a motionless crack exhibiting the transformational process zone at its tip within the field-theoretical approach. The latter enables us to describe the transformation toughness phenomenon and relate it to the solid's location on its phase diagram. We demonstrate that the zone extends backward beyond the crack tip due to the zone boundary surface tension. This setback engenders the crack-tip shielding, thus forming the transformation toughness. We obtain a quadrature expression for the effective fracture toughness using two independent approaches—(i) with the help of the elastic Green function and, alternatively, (ii) using the weight functions—and calculate it numerically applying the results of our simulations. Based on these findings, we derive an accurate analytical approximation that describes the transformation toughness. We further express it in terms of the experimentally accessible parameters of the phase diagram: the hysteresis width, the phase transition line slope, and the transformation strain.

DOI: [10.1103/PhysRevE.103.023001](https://doi.org/10.1103/PhysRevE.103.023001)

I. INTRODUCTION

A. Transformational process zones at the crack tips

Stress concentration at the tip of a brittle crack impacts the solid state, gives rise to various nonlinear phenomena that influence the crack's static and dynamic properties. One of them is the formation of the *transformation process zone* (also referred to here as the *zone*). Within the zone, the solid exhibits a phase which differs from that in bulk.

Observations of zones have been reported for many materials of various chemical compositions such as some metals [1]; transformation-induced plasticity (TRIP) steels [2,3]; shape memory alloys [4]; metallic glasses [5]; dielectric monocrystals [6,7]; ferroelectric ceramics [8–10]; ZrO₂ monocrystals, ceramics, and composites [11–14]; and the two-dimensional (2D) nanocrystal MoWSe₂ [15]. Superconductive zones have also been observed in high- T_c superconductors [16]. Observations of process zones in polymers and resins have been also reported [17].

The modern instruments that have been developed during the last decade—such as high resolution synchrotron scattering [18], high-angle annular dark-field scanning transmission electron microscopy [19], electron nanodiffraction [20], scanning electron microscopy with backscatter diffraction [21,22], high-resolution x-ray microdiffraction [23], and atomic force microscopy [24,25] to name a few—enable the direct observation of the zone, at least at the tip of a motionless or slowly propagating crack.

A correlation has been established between the process zone formation and the fracture toughness's improvement, referred to as the *transformation toughness*. Its observation has been reported in TRIP steels [2], stishovite [26], zirconia

ceramics [11,27–30], and ceramic composites containing zirconia components [31]. This has engendered a keen interest to understand the origin of the transformation toughness.

B. Theoretical analysis of process zones

In the theoretical studies of transformational process zones computational, mechanical, and field-theoretical approaches can be pointed out.

1. Computational approach

The atomistic mechanisms of local phase transformations have been studied by computer simulations and density-functional-theory-like calculations for several solids, such as iron [32], amorphous metal [33], silicon [34,35], tantalum [36], zirconium [37], ZrO₂ [38], UO₂ [39], molybdenum [20], Bi₂NiAl [40], and nitinol [41]. This has become possible thanks to the development of computational power accompanied by the advance of molecular dynamics and the implementation of hybrid approaches that combine molecular dynamics with quantum mechanics [35,42].

Simulations have revealed a strong dependence of the zone formation upon (i) the loading mode, (ii) the crack plane direction, and (iii) the sample geometry [32,43]. They have further elucidated the atomistic mechanisms leading to the development of a process zone [35,43].

2. Mechanical approach

Many papers have formulated the *mechanical approach*, based on the assumptions that (i) the zone only differs from the rest of the solid by its elastic modules and the existence of a spontaneous strain, and (ii) a simple invariant relation imposed on stress tensor components determines the zone-matrix interface. This approach has enabled the description of the process zone as an “elastic washer” that is produced

*Corresponding author: aboulbitch@gmx.de

from a different material and inserted into the matrix orifice with a preload. Within these assumptions one treats the zone as a purely mechanical problem with the moving boundary [13,44–47].

Antolovich was the first to explain the transformation toughness within a simplified mechanical approach [2]. He included the energy of the wake, the long-living metastable layer, to the fracture energy, thus explaining the growth of the fracture toughness. Antolovich approach was followed in many succeeding papers [27–30].

By analyzing the transformation toughness in a material exhibiting a phase transition with a dilatant transformation strain, McMeeking and Evans have proposed a *mechanical shielding* [48] accounting for the compression taking place within the wake: the latter opposes the crack opening. Budiansky *et al.* analyzed this mechanism in a composite with particles exhibiting stress-induced transformation [49]. Rose discovered [50] and, while using Hutchinson's approach [51], Stump and Budiansky studied in detail the divergence of the process zone referred to as the *resonance* [52]. These papers used the phase boundary criterion $\sigma_{ii} = \sigma_m$, where σ_{ii} is the spur of the stress tensor and σ_m is its critical value regarded as a material constant. With these assumptions, the process zone has a cardioid form and does not contribute to the transformation toughness [48,49].

Papers [53,54] analyzed a model in which the criterion accounts for both dilatant and shear stresses. We will discuss some of these assumptions and criteria in more detail in Sec. VIII. Budiansky and coworkers developed a model that focuses on the shear strain within spherical ZrO_2 inclusions embedded into the elastic matrix by regarding the tetragonal to monoclinic transition as a proper ferroelastic one [55,56].

A detailed review up to the year 2003 one finds in the paper of Kelly and Rose [13].

In all above papers [2,27,28,30,48–50,52] the authors assumed the crack to propagate quasistatically, while regarding the phase transformation as irreversible. These two conditions ensured the formation of the long-living wake contacting the crack surfaces behind its tip. The latter gives rise to mechanical shielding contributing to the transformation toughness.

More recent papers focused on the crack-tip phase transformations in the shape memory alloys such as NiTi, and steels. Freed and Banks-Sills [57] developed a theoretical approach to shape memory alloys accounting for the temperature shift of the boundary criterion. Baxevis *et al.* pointed to the path dependence of the J integral and addressed the influence of the transformation on the ratio of the far-field-energy to the crack-tip-energy release rates [58,59]. Ma, Korsunsky, and McMeeking described the transformation toughening in anisotropic solids [60]. Lexcellent and Thiebaud [61] analyzed NiTi, while focusing on the asymmetry between tension and compression. The transformation in this material at the crack tip has been addressed in several papers [41,62]. Maletta and Young developed a model of the NiTi process zone accounting for the stress triaxiality [63]. Krupp *et al.* analyzed the extent of the martensite ahead of the crack tip in metastable austenite steel depending on the crack length [64]. Vatne *et al.* addressed the crack-tip bcc-fcc transformation in Fe [65]. Toughening in bulk metallic glasses has been studied

in [66]. The papers [67] numerically addressed the process zones in various zirconia ceramics.

Let us particularly note that some papers have developed analytical approaches using the Green function method [60,68,69] to describe the process zone because it is an important instrument also used in this paper.

3. Field-theoretical approach

Let us first note that the phenomenological criteria of the phase boundary hypothesized in most of the papers listed above were inspired by those used in plasticity. However, when applied to phase transformations, they are physically not grounded. The use of the well-founded criteria [70–72] leads to a different process zone configuration, as we discuss in detail later on.

Second, the phase transformation *irreversibility* that is fundamental for the papers [13,48–50,52], is a rather exotic phenomenon (see Sec. VIII E 3). Indeed, in most solids, the interface between the stable and metastable phases propagates with a finite velocity, resulting in the decrease of the volume occupied by the metastable phase [73].

These two points suggest a different transformation toughness scenario.

These reasons motivated us to formulate this problem within the field-theoretical approach. Within the latter, we describe the zone by the field of the order parameter $\eta = \eta(\mathbf{R})$. Here $\mathbf{R} = (X, Y)$, where X and Y are the spatial in-plane coordinates. As in the classical Landau theory of phase transitions [74], it represents a set of internal degrees of freedom of the solid. They determine the difference between the crystal structures and symmetries of the mother and daughter phases, and $\eta(\mathbf{R})$ obeys a well-established equation of state, the Ginzburg-Landau equation [see Eq. (26), Sec. III]. Within this approach, both the process zone boundary and the transformation reversibility straightforwardly follow from the solution of the equation of state.

The field-theoretical approach has been pioneered by Nabutovsky and Shapiro [75] who described a superconducting “filament” at a dislocation. In the paper [68] one of us first adopted this approach to address the crack-tip zone. Later it was developed in [76–82] as well as in the paper [83]. A few recent papers applied the phase-field approach to cracks combining it with the field-theoretical paradigm. It also proved useful in studying the process zone in ferroelectrics [84]. This combination was used in [85] to determine the strain and stress fields and the zone configuration at the crack tip. Zhao *et al.* studied the structure of a polydomain zone at the initial stage of the crack propagation by combining the field-theoretical approach with the phase-field method [86]. Zhu and Luo applied such a combination to study nucleation of the intergranular microcracking addressing polycrystalline, tetragonal zirconia [87]. Levitas and coworkers studied the effect of wetting of crack surfaces by the zone [88] and the capillary phenomenon due to the interaction of the phase-field gradients with the strain field [89]. However, these papers do not discuss the transformation toughness problem.

Within the field-theoretical approach, we addressed the process zone formed by the structural phase transformation, the mother and daughter phases possessing different struc-

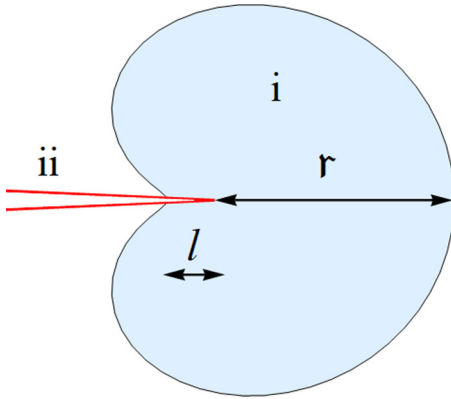


FIG. 1. Schematic view of the process zone at the tip of a motionless or slowly propagating crack. The zone width r and the contact length l are indicated.

tures of their crystal lattices [68,76–82]. We assumed that the mother phase exhibits a high symmetry group, while the group of the daughter phase is its subgroup. One can treat this case within the Landau theory of phase transitions [74]. The zone description differs from the classical Landau theory of the bulk solids [74] in one essential aspect: it is the highly inhomogeneous stress in the vicinity of the crack tip that induces the transition from the bulk mother phase to the daughter phase localized within the process zone. Therefore, the order parameter distribution is also highly inhomogeneous. Within the zone, one finds $\eta = \eta(\mathbf{R}) \neq 0$. Far from the tip, the asymptotics $\eta(\mathbf{R}) \rightarrow 0$ holds, corresponding to the mother phase.

Previously [77], we have shown that at high temperatures, T , or low value of the stress intensity factor, K_I , no zone takes place at the crack tip. By decreasing T , the zone emerges upon achieving some critical temperature $T_* = T_*(K_I)$. At $T < T_*$ the crack tip exhibits the transformational process zone [71,77]. Analogously, at a fixed temperature T , the zone emerges as soon as the stress intensity exceeds the critical value $K_I \geq K_* = K_*(T)$.

We recently demonstrated [72,81] that at the tip of a motionless crack the zone shape is almost everywhere close to the cardioid, but essentially differs from it in its back. This difference will be discussed in Sec. V A. At the tip of a slowly propagating crack, the zone exhibits a concave shape with an invagination in its trailing part. Figure 1 schematically shows the process zone (i) at the tip of the motionless or slowly propagating crack (ii). In the slow crack propagation regime, the wake completely “melts down.” Thus, the quasistatic crack propagation ($V \rightarrow +0$) allows no wake. Therefore, the wake-based mechanisms cannot explain the transformation toughness phenomenon, and the problem of defining the physical reasons for the transformation toughness in crystals and its impact stays open.

(a) *This paper.* This paper aims to reveal the physical origin of the transformation toughness in crystals and study its mechanism free of the hypotheses of the transformation irreversibility and the quasistatic crack propagation.

We report a self-consistent, field-theoretical model describing a crack’s process zone in an elastically isotropic crystal. We show that this zone generates the transformation tough-

ness even in the case of the motionless crack. It does not need to propagate. The field-theoretical approach enables us to relate this phenomenon to the position of the solid in its phase diagram.

We start with the derivation of a system of field-theoretical equations defining the motionless crack with the process zone at its tip, which is valid for a broad class of solids. Next, we eliminate the elastic variables from this system. Thus, we obtain the process zone equation only in terms of the order parameter, demonstrating that it exhaustively describes the crack-zone ensemble. Next, we derive an expression for the stress intensity factor for such a crack which depends on a single dimensionless parameter ζ_0 . We first obtain the value of this parameter using our previous simulation results. On this basis, we further obtain an accurate analytical approximation for the transformation toughness for a motionless crack. Then, we demonstrate that one expresses the relative perturbation of the fracture toughness in terms of the product of two dimensionless variables: s only depending on the position in the phase diagram and Δ defining the toughening intensity. We, finally, show that Δ is proportional to the ratio $\Delta T_b / \Delta T_h$, where ΔT_h is the hysteresis width and ΔT_b is the shift of the transformation temperature under the applied transformation stress.

(b) *The structure of this paper.* In Sec. II, we derive a system of equations for the crack-zone ensemble. In Sec. III, we eliminate the elastic variables and derive the process zone equation. In this section, we also introduce the self-consistency condition. In Sec. IV, we pass to dimensionless variables convenient for the numerical solution. In Sec. V, we recite a part of the results of our simulations [72,81] which are necessary for the present paper. In Sec. VI, we derive an equation for the stress intensity factor. We do this within the Green function approach in Sec. VIA and alternatively using the weight functions in Sec. VIB to numerically obtain the value of ζ_0 in Sec. VIC. We further derive an accurate analytical approximation for ζ_0 . On this basis, we analytically obtain the expression for the transformation toughness in Sec. VII. Section VIII contains a discussion. Here we discuss the physical origin of the order parameter, and list the limitations of our approach and its generalizations. We further compare our results to the previous ones, review the possible physical origins of long-living wakes, and relate the mechanical “resonance” of Rose to the position on the phase diagram. Finally, we reveal the physical origin of fracture toughness perturbation and give estimates of its typical values. In Appendix A, we give details of the numerical methods and the estimates of the integrals yielding ζ_0 . Appendix B communicates the derivation of the analytical expression for the contact length l (defined in Fig. 1), which enables us to obtain ζ_0 analytically.

II. FIELD-THEORETICAL EQUATIONS DESCRIBING THE CRACK-ZONE COMPLEX

A. The free energy

In this paper, we focus on the case of a structural phase transformation generating the process zone at the crack tip. In this case, the order parameter η is a normal coordinate of an optical phonon (see Sec. VIIIA for its more detailed

description). The order parameter $\eta(\mathbf{R}) \neq 0$ contributes to the solid's free energy \mathfrak{F} in the following way:

$$\mathfrak{F} = \mathfrak{F}_0 + \int_{\Omega} \Phi(\eta, \boldsymbol{\varepsilon}) d\Omega \quad (1)$$

where \mathfrak{F}_0 is the free energy of a solid containing a crack without a process zone, and $d\Omega = dXdY$ is the area element. Here X and Y are the in-plane coordinates, and Ω is the infinite plane. In the expression (1), we assign the integral to the unit length in the Z direction. $\Phi = \Phi(\eta, \boldsymbol{\varepsilon})$ is the free energy density of the process zone, and $\boldsymbol{\varepsilon} \equiv \varepsilon_{ik}$ is the strain tensor:

$$\varepsilon_{ik} = \frac{1}{2} \left(\frac{\partial u_i}{\partial X_k} + \frac{\partial u_k}{\partial X_i} \right). \quad (2)$$

Here the vector $u_i = u_i(X, Y)$ also denoted as $\mathbf{u}(\mathbf{R})$ is the displacement vector. Note that it should not be confused with the rescaled order parameter, $u(x, y, \tau)$, used in the following.

One can regard the free energy density as a molecular potential for nonlinear atomic vibrations in terms of the normal coordinate η , and write it down in the following form:

$$\Phi(\eta, \varepsilon_{ik}) = \Phi_{\text{pt}}(\eta) + \Phi_{\text{el}}(\boldsymbol{\varepsilon}) - A\eta^2 \varepsilon_{ii}. \quad (3)$$

Here the function $\Phi_{\text{pt}}(\eta)$ denotes the part responsible for the phase transition in the stress-free solid. One can represent $\Phi_{\text{pt}}(\eta)$ as a polynomial in terms of even powers of the order parameter η and its gradient $\nabla\eta$ [74]. Given that we aim to describe a first-order transition, the polynomial must be at least the sixth order:

$$\Phi_{\text{pt}} = \frac{g}{2} (\nabla\eta)^2 + \frac{\alpha}{2} \eta^2 + \frac{\beta_0}{4} \eta^4 + \frac{\gamma}{6} \eta^6. \quad (4)$$

Here $g > 0$ and $\gamma > 0$ are the parameters of the Landau potential (1). If $\beta_0 < 0$, then the potential (4) describes the first-order phase transition between the mother phase $\eta = 0$ and the daughter phase $\eta \neq 0$. It is this case that we address in the present paper. In accord with the classical Landau theory we assume that only the factor α depends on the temperature:

$$\alpha = \alpha_0(T - T_{c0}) \quad (5)$$

where $\alpha_0 > 0$ is a constant, T is the temperature, and T_{c0} is the Curie temperature at zero pressure.

We do not examine here the justification of the free energy (4). It has been discussed in numerous papers and textbooks. In the case of homogeneous crystals, the description of the second-order phase transformations ($\beta_0 > 0$, $\gamma > 0$, or $\gamma = 0$) one finds in, e.g., [74,90], and [91]. The discussion of the first-order phase transformations with the potential (4) ($\beta_0 < 0$, $\gamma > 0$) one finds in [90,91]. For more complex cases with multicomponent order parameters and the Landau polynomial of the order higher than 6, we refer the reader to the book [92,93].

Furthermore, $\Phi_{\text{el}}(\boldsymbol{\varepsilon})$ is the elastic part of the free energy density, and here we use the elastically isotropic approximation:

$$\Phi_{\text{el}} = \frac{\lambda}{2} \varepsilon_{ii}^2 + \mu \varepsilon_{ik}^2 \quad (6)$$

where $\lambda = E\nu/(1+\nu)(1-2\nu)$ and $\mu = E/2(1+\nu)$ are Lamé coefficients, μ is the shear modulus, E is Young's modulus, and ν is Poisson's ratio.

The limitation with the square terms $\Phi_{\text{el}} \sim \boldsymbol{\varepsilon}^2$ implies that we assume that the elastic nonlinearity plays a negligible role.

In contrast, the nonlinearity related to the order parameter (4) is essential. This assumption is valid for many inorganic solids. Let us note that it fails for the essentially elastically nonlinear solids such as ferroelastics [94] or brittle gels [95].

Finally, the contribution $A\eta^2 \varepsilon_{ii}$ to (3) takes into account the coupling between the strain and order parameter fields. It is worth commenting that the form of the term $A\eta^2 \varepsilon_{ii}$ in (3) implies that the phase transition only gives rise to a *transformation strain* that is a pure dilatation, while no spontaneous shear strain takes place. Whether an increase in the volume or its decrease takes place during the transformation depends on the sign of the *striction constant* A . For $A < 0$, the process zone only emerges below the bulk phase transition temperature, T_b . At $A > 0$, it appears at $T > T_b$ [77]. It is this latter case, $A > 0$, that we focus on here. Within the process zone, the *transformation dilatation* generates the stress referred to here as the *transformation stress*.

Let us observe that in a homogeneous solid with no crack, one can unify the terms $\sim \eta^2$ in the free energy density (3) and (4) in the following way:

$$\Phi(\eta, \varepsilon_{ik}) = \frac{\alpha_0}{2} \left(T - T_{c0} - \frac{2A\varepsilon_{ii}}{\alpha_0} \right) \eta^2 + \frac{1}{4} \beta_0 \eta^4 + \frac{1}{6} \gamma \eta^6 + \Phi_{\text{el}}(\boldsymbol{\varepsilon}).$$

Let us express the dilatation ε_{ii} in terms of the hydrostatic pressure $p = -\sigma_{ii}/3$ as follows: $\varepsilon_{ii} = -3(1-2\nu)p/E$. This representation enables us to define the pressure-dependent Curie temperature $T_c(p)$:

$$T_c(p) = T_{c0} - \frac{3(1-2\nu)A}{\alpha_0 E} p. \quad (7)$$

We make use of this expression below.

The parameters of the Landau potential g , α_0 , β_0 , T_{c0} , and A related to the phase transformation together with the elastic constants E and ν constitute a set of material constants of the solid that control both its phase transformations and fracture behavior.

B. Equations of state

By variation of the free energy \mathfrak{F} (1) with respect to the order parameter η and displacement vector \mathbf{u} one derives the equations of state:

$$g\Delta\eta - [\alpha - 2A\varepsilon_{ii}(\mathbf{R})]\eta - \beta_0\eta^3 - \gamma\eta^5 = 0$$

$$\partial\sigma_{ik}/\partial X_k = 0 \quad (8)$$

Here $\Delta = \partial^2/\partial X^2 + \partial^2/\partial Y^2$ is the 2D Laplace operator. The term $\sim \varepsilon_{ii}\eta$ in the first equation (8) accounts for the interaction of the soft mode η with the strain field of the solid. Alternatively, one can regard it as the interaction between the acoustic and optical phonons. Furthermore, σ_{ik} is the stress tensor defined as $\sigma_{ik} = \partial\Phi/\partial\varepsilon_{ik}$, which takes the following form:

$$\sigma_{ik} = \lambda\varepsilon_{jj}\delta_{ik} + 2\mu\varepsilon_{ik} - A\eta^2\delta_{ik}. \quad (9)$$

Here δ_{ik} is the Kronecker symbol, and the last term in (9) describes the transformation stress generated by the phase transition.

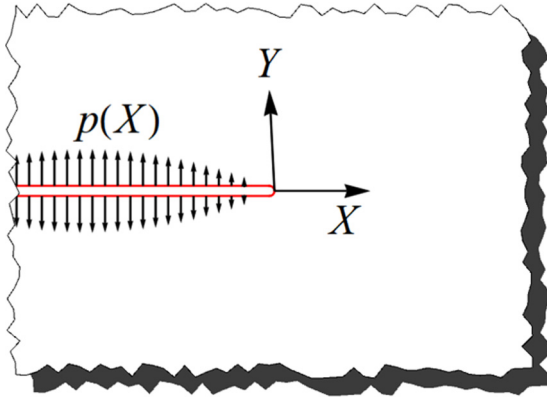


FIG. 2. Illustration to the mechanical boundary conditions. A fragment of an infinite plane with a semi-infinite crack loaded normally to its surface by the force $p(X)$. The origin of coordinates is placed in the crack tip.

C. Statement of the problem

1. Boundary conditions

A system of equations (8) and (9) describes a more general range of phenomena than only the crack-tip process zone, such as the condensation of soft phonons, and magnetic or superconductive states at dislocations [96] and others.

The crack-process zone complex is a particular case obeying this system, and its specificity manifests itself in the boundary conditions.

Keeping in mind that we aim to describe the process zone localized in the close vicinity of the crack tip while vanishing afar, we use the zero Dirichlet condition at the outer boundary $\partial\Omega$ of the domain Ω :

$$\eta|_{\partial\Omega} = 0. \quad (10)$$

One also needs to define the boundary condition for the order parameter at the crack's surfaces $\partial\Omega_{\text{crack}}$. Here we use the so-called natural boundary condition:

$$(\mathbf{n} \cdot \nabla \eta)|_{\partial\Omega_{\text{crack}}} = 0 \quad (11)$$

where \mathbf{n} is the unit vector normal to the crack surfaces $\partial\Omega_{\text{crack}}$.

Depending on specific properties of the material and the state of the fracture surface a few other types of boundary conditions at $\partial\Omega_{\text{crack}}$ are also plausible, such as in the case of the wetting of the crack surface by the daughter phase [88,89]. However, a discussion of such boundary conditions is out of the scope of this paper.

Let us turn to the statement of the mechanical problem. We consider a semi-infinite crack spanning from $X = -\infty$ to 0 in the infinite plane. The crack is only loaded by a force $p(X)$ ($X < 0$) that is normally and symmetrically applied to both its surfaces, as shown schematically in Fig. 2.

2. A high-temperature solution and bifurcation

At high temperatures, T , or low value of the crack load, only the solution $\eta(\mathbf{R}) \equiv 0$ of (8) is stable. This corresponds

to no zone at the crack tip. The stress intensity factor has the classical form

$$K_I^{(\text{ap})} = \sqrt{\frac{2}{\pi}} \int_0^\infty \frac{p(-X)}{\sqrt{X}} dX \quad (12a)$$

referred to here as the *applied stress intensity factor*. Here ‘‘ap’’ in the superscript stands for ‘‘applied.’’ It generates the classical stress and strain distributions around the tip. The applied stress intensity factor gives rise to the solution known from the linear elastic fracture mechanics with the displacement vector $u_i^{(0)}$ ($i = 1, 2$) in the standard form [97]:

$$u_i^{(0)} = \frac{K_I^{(\text{ap})}}{\mu} \sqrt{\frac{R}{2\pi}} \varphi_i(\theta) \quad (13)$$

with

$$\varphi_i(\theta) = \begin{cases} \cos(\theta/2)[1 - 2\nu + \sin^2(\theta/2)], & i = 1 \\ \sin(\theta/2)[2 - 2\nu - \cos^2(\theta/2)], & i = 2 \end{cases} \quad (14)$$

Here $R = \sqrt{X^2 + Y^2}$ and $\theta = \arctan(Y/X)$ are the polar coordinates with the origin at the crack tip. Within the linear elastic fracture mechanics (13) and (14) give rise to the classical expression for the crack-tip strain $\varepsilon_{ij}^{(0)}$ [97].

Below a certain temperature $T = T_*(K_I^{(0)})$, the system of equations (8) and (9) exhibits a bifurcation. The mother-phase solution $\eta \equiv 0$ becomes unstable and a new stable solution $\eta(\mathbf{R}) \neq 0$ with $\eta(\infty) = 0$ arises. This solution describes a crack-tip zone embedded into the mother-phase matrix. The temperature of the zone formation T_* lies above the spinodal of the bulk phase transition [71]. Further details can be found in the paper [77].

D. Bueckner's approach revisited

The transformation from the zoneless crack to that possessing the zone gives rise to the transformation strain. The latter adds to $\varepsilon_{ij}^{(0)}$ and, correspondingly, forms a supplementary stress distribution around the crack tip. This stress contributes to the load experienced by the crack and, thus, perturbs the stress intensity factor. The net stress intensity factor K_I takes the following form:

$$K_I = K_I^{(\text{ap})} + \delta K_I. \quad (15)$$

Within the present approach, we determine this perturbation in a self-consistent way.

Let us observe that the transformation stress term $-A\eta^2\delta_{ik}$ in Eq. (9) can be interpreted as the bulk force, $\mathbf{f} = (f_1, f_2, 0)$, with the components

$$f_i = -A \frac{\partial \eta^2}{\partial X_i} \quad (i = 1, 2). \quad (16)$$

One can regard it as if the zone generates the force (16) in all its points. To cope with such forces, one can use the approach put forward by Bueckner, enabling one to convert the load applied somewhere to the body to the force distributed along the crack's surface [98] (see also [99]). One performs this approach in two steps.

During the first step, one considers a hypothetical crack-free body to which bulk forces are applied. One then

determines its stressed state. Following Muschelivili [99], we refer to this state as the *first stressed state*.

During the the second step, one calculates the stress of the first stressed state in the points of the crack surface and uses it to determine the perturbation of the stress intensity factor.

III. ELIMINATION OF ELASTIC VARIABLES

Expression of the elastic variables in terms of the order parameter distribution

By directly applying Bueckner's idea to the crack with the process zone, we observe that the displacement vector u_i comprises two contributions:

$$u_i(\mathbf{R}) = \tilde{u}_i(\mathbf{R}) - A \iint_{\Omega} G_{ij}(\mathbf{R} - \mathbf{R}') \frac{\partial \eta^2(\mathbf{R}')}{\partial X'_j} d\Omega'. \quad (17)$$

Here $G_{ij}(\mathbf{R} - \mathbf{R}')$ is the elastic Green function of the solid with no crack, $d\Omega' = dX'dY'$, and we use the Einstein summation convention.

The expression (17) is the solution of the elastic part of the problem in terms of the derivatives of the order parameter distribution $\partial \eta^2 / \partial X_j$. The second term (17) describes the displacements in the whole body generated by the phase transformation within the zone.

The first term describes crack contribution. In the classical Green function theory, one takes the first term in (17) in the form $\tilde{u}_i = u_i^{(0)}$ (13). It then describes the contribution of the bare crack with no process zone.

However, as soon as the process zone arises, taking $\tilde{u}_i = u_i^{(0)}$, one only accounts for a part of the crack contribution to the displacements. Indeed, the zone generates transformation stress in the whole body described by the second term (17). This stress exerts a load on the crack's surfaces. The latter adds to the originally applied one, $p(X)$ (Fig. 2). It, thus, contributes to the perturbation of the stress intensity factor. For this reason, in the expression for (17) instead of $u_i^{(0)}(\mathbf{R})$ (13), we use the expression $\tilde{u}_i(\mathbf{R})$ in which one replaces the original stress intensity factor $K_I^{(\text{ap})}$ by its perturbed value K_I according to (15):

$$\tilde{u}_i(\mathbf{R}, \theta) = \frac{K_I}{\mu} \sqrt{\frac{R}{2\pi}} \varphi_i(\theta) \quad (i = 1, 2) \quad (18)$$

with $\varphi_i(\theta)$ given by (14).

In the present problem, the latter replacement represents a *self-consistency condition*. Let us stress that while we started with using the Green function of the intact elastic plane, the replacement $K_I^{(\text{ap})} \rightarrow K_I$ accounts for the crack presence in it. The solution (17), therefore, describes the solid with the crack-zone complex, rather than mechanistically unifying the bare crack with the hypothetical "crack-free zone." The solution becomes complete. One can regard this procedure as the "upgrading" of the Green function of the crack-free solid to the case of one containing the crack.

One finds the strain tensor in the following form:

$$\begin{aligned} \varepsilon_{il}(\mathbf{R}) = & \tilde{\varepsilon}_{il}(\mathbf{R}) - \frac{A}{2} \iint_{\Omega} \left[\frac{\partial G_{ij}(\mathbf{R} - \mathbf{R}')}{\partial X_l} + \frac{\partial G_{lj}(\mathbf{R} - \mathbf{R}')}{\partial X_i} \right] \\ & \times \frac{\partial \eta^2(\mathbf{R}')}{\partial X_j} d\Omega'. \end{aligned} \quad (19)$$

In the expression (19), $\tilde{\varepsilon}_{il}(\mathbf{R})$ is the strain generated by the crack. It originates from the displacements \tilde{u}_i (18) according to (2). In the following, we only use its spur, which we therefore write here in the explicit form:

$$\tilde{\varepsilon}_{ii}(\mathbf{R}) = \frac{2(1-2\nu)(1+\nu)K_I}{E(2\pi R)^{1/2}} \cos(\theta/2). \quad (20)$$

K_I stays here, instead of $K_I^{(\text{ap})}$, as in (18), according to the self-consistency condition.

It is convenient to introduce the Fourier transform of the square of the order parameter, $\eta^2(\mathbf{R})$:

$$\begin{aligned} \eta^2(\mathbf{R}) &= \iint Q(\mathbf{k}) \exp(i\mathbf{k}\mathbf{R}) \frac{d^2k}{(2\pi)^2}; \\ Q(\mathbf{k}) &= \iint \eta^2(\mathbf{R}) \exp(-i\mathbf{k}\mathbf{R}) d^2R \end{aligned} \quad (21)$$

where the bold \mathbf{k} is the vector of the reciprocal space. One should not confuse it with its in-plane components k_i , such that $\mathbf{k} = (k_1, k_2)$ and its scalar absolute value $k = (k_1^2 + k_2^2)^{1/2}$ met in the expressions below. We also use the Fourier transform of the elastic Green function $G_{ij}(\mathbf{k}) = \iint G_{ij}(\mathbf{R}) \exp(-i\mathbf{k}\mathbf{R}) d^2R$:

$$G_{ij}(\mathbf{k}) = \frac{2(1+\nu)}{E} \left[\frac{\delta_{ij}}{k^2} - \frac{k_i k_j}{2(1-\nu)k^4} \right]. \quad (22)$$

One finds the integral representation of the dilatation, $\varepsilon_{ii}(\mathbf{R})$:

$$\varepsilon_{ii}(\mathbf{R}) = \tilde{\varepsilon}_{ii}(\mathbf{R}) + A \iint k_i k_j G_{ij}(\mathbf{k}) Q(\mathbf{k}) \exp(i\mathbf{k}\mathbf{R}) \frac{d^2k}{(2\pi)^2}. \quad (23)$$

Let us observe that the following identity holds:

$$G_{ij}(k) k_i k_j = \frac{(1-2\nu)(1+\nu)}{E(1-\nu)}. \quad (24)$$

Substitution of this relation into (23) simplifies the latter. Comparing it with (21) one finds

$$\begin{aligned} \iint k_i k_j G_{ij}(\mathbf{k}) Q(\mathbf{k}) \exp(i\mathbf{k}\mathbf{R}) \frac{d^2k}{(2\pi)^2} &= \frac{(1-2\nu)(1+\nu)}{E(1-\nu)} \\ &\times \iint Q(\mathbf{k}) \exp(i\mathbf{k}\mathbf{R}) \frac{d^2k}{(2\pi)^2} \equiv \frac{(1-2\nu)(1+\nu)}{E(1-\nu)} \eta^2(\mathbf{R}) \end{aligned}$$

yielding the exact expression for $\varepsilon_{ii}(\mathbf{R})$:

$$\begin{aligned} \varepsilon_{ii}(\mathbf{R}) &= \frac{2(1-2\nu)(1+\nu)K_I}{E(2\pi R)^{1/2}} \cos(\theta/2) \\ &+ \frac{A(1-2\nu)(1+\nu)}{E(1-\nu)} \eta^2(\mathbf{R}) \end{aligned} \quad (25)$$

where the first term in the right-hand part represents $\tilde{\varepsilon}_{ii}(\mathbf{R})$ given by the classical expression (20) of the linear elastic fracture mechanics, while the second one describes the contribution of the zone dilatation.

Finally, the substitution of the dilatation (25) into (8) yields the zone equation. This is the nonlinear equation of state in terms of the order parameter:

$$g\Delta\eta - \left[\alpha - B \frac{\cos(\theta/2)}{\sqrt{R}} \right] \eta - \beta\eta^3 - \gamma\eta^5 = 0 \quad (26)$$

where for the sake of compactness, we introduce a new parameter B expressed in terms of a combination of material

constants and the perturbed stress intensity factor K_I :

$$B = \frac{4A(1-2\nu)(1+\nu)}{\sqrt{2\pi E}} K_I \quad (27)$$

and instead of β_0 we now use its modified value β :

$$\beta = -\left(|\beta_0| + \frac{2A^2(1-2\nu)(1+\nu)}{E(1-\nu)}\right) < 0. \quad (28)$$

Let us note that the coordinate-dependent expression $B \cos(\theta/2)R^{-1/2}$ in (26) originates from the first term in the right-hand part of (25). It describes the effect of the inhomogeneous strain field on the order parameter. The second term in the right-hand part of (25) participates in the modification of the parameter β (28).

The zone equation (26) self-consistently describes the order parameter distribution at the crack tip engendered by the net near-field strain. The latter represents the combined contribution of the crack and process zone.

Furthermore, the only dependent variable of (26) is $\eta(\mathbf{R})$, and no elastic variables are involved. One concludes that the solution of (26) exhaustively describes the process zone at the crack tip. Provided that the (26) solution has been obtained, it is possible to describe the fracture toughness. This task will be addressed later on.

IV. RESCALING

For further study, it is convenient to rescale the variables to make Eq. (26) dimensionless. This will enable us to decrease the number of control parameters of (26), thus simplifying the numerical study. Even more important, it will later enable us to obtain a closed expression for the perturbed fracture toughness.

Rescaling Eq. (26)

Let us pass from the physical coordinates X and Y and the order parameter, $\eta(X, Y)$, to the dimensionless ones x , y and $u = u(x, y)$ as follows:

$$\begin{pmatrix} X \\ Y \end{pmatrix} = R_0 \begin{pmatrix} x \\ y \end{pmatrix}, \quad \eta = \eta_0 u \quad (29)$$

where R_0 is the intrinsic scale of the problem, and η_0 is the characteristic value of the order parameter. They are expressed as follows:

$$R_0 = \frac{1}{2^{1/3}} \left(\frac{g}{B}\right)^{2/3}, \quad \eta_0 = \frac{B^{1/3}}{2^{1/6} \gamma^{1/4} g^{1/12}}. \quad (30)$$

Their origin has been discussed in detail in [77] and [72].

Substitution of (30) into Eq. (26) yields the following equation:

$$\Delta u - [a - U(x, y)]u + bu^3 - u^5 = 0 \quad (31)$$

with the boundary conditions $u|_{\partial\Omega} = 0$ and $(\mathbf{n} \cdot \nabla u)|_{\partial\Omega_{\text{crack}}} = 0$.

Here $\Delta u = \partial^2 u / \partial x^2 + \partial^2 u / \partial y^2$ and $\nabla u = (\partial u / \partial x, \partial u / \partial y)$ are the 2D Laplacian and gradient of u in terms of the dimensionless coordinates

$$U(x, y) = \frac{[(x^2 + y^2)^{1/2} + x]^{1/2}}{(x^2 + y^2)^{1/2}} = \frac{\sqrt{2} \cos(\theta/2)}{r^{1/2}} \quad (32)$$

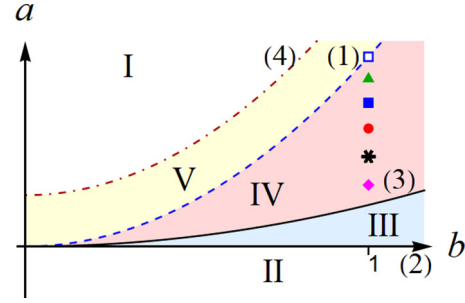


FIG. 3. Plane of the dimensionless parameters (b , a) divided into domains with different behaviors of Eqs. (3) and (4). We simulated Eq. (31) in the domain IV at $b = 1$. The points where the simulations have been performed are shown as follows: $a = 0.20$ (diamond), 0.21 (asterisk), 0.22 (disk), 0.23 (filled square), 0.24 (triangle), and 0.25 (open square).

where $r = (x^2 + y^2)^{1/2}$ and $\theta = \arctan(y/x)$ are dimensionless cylindrical coordinates.

Equation (31) depends on two dimensionless control parameters, a and b . They are related to the parameters of the potentials (4) and (6) α , β , γ , and others as follows:

$$a = \frac{2^{2/3} g^{1/3}}{B^{4/3}} \alpha, \quad b = -\frac{2^{1/3} g^{1/6}}{B^{2/3} \gamma^{1/2}} \beta. \quad (33)$$

Let us recall that $\beta < 0$ describing the first-order transition corresponds to $b > 0$. In this paper, we will only consider the case $\alpha > 0$. This corresponds to $a > 0$.

Equation (31) can be conveniently solved numerically.

V. NUMERICAL RESULTS

A. The phase diagram

Figure 3 shows the plane of parameters (b , a). It is divided into domains where the free energy (3) and (4) exhibits different structure and, correspondingly, Eq. (31) has solutions of different types. Let us observe that a and b depend on thermodynamic parameters such as temperature T and pressure p , temperature and concentration, or any other pair. Therefore, the (b , a) plane maps on the plane of the two thermodynamic parameters, such as the (p , T) plane. The latter represents the phase diagram of the solid. Let us mention that this mapping is standard in the Landau theory of phase transitions [90,92]. Consequently, we refer to Fig. 3 as the phase diagram.

Let us briefly describe the phase diagram. The pure mother phase with no crack-tip process zone takes place in domain I, while the pure daughter phase occupies the domain II. In domains III and IV, the mother and daughter phases coexist: the mother phase being metastable and the daughter stable in the domain III. In contrast, the mother phase is stable and the daughter phase is metastable in domain IV.

Domain IV is flanked by the upper spinodal

$$a_{\text{up}} = \frac{b^2}{4} \quad (34)$$

on its top (shown in Fig. 3 by the dashed line 1), and by the binodal

$$a_{\text{b}} = \frac{3b^2}{16} \quad (35)$$

at its bottom (solid line 3). Domain III is bounded by the lower spinodal $a_{\text{low}} = 0$ from below (line 2 in Fig. 3). These two domains are separated from one another by the binodal a_b . On the binodal, the mother phase's free energy density equals that of the daughter phase.

Finally, at line 4 (the dot-dashed line in Fig. 3) Eq. (31) exhibits a bifurcation. Below this line, the process zone emerges at the crack tip. Thus, it only exists above line 3. The zone consists of the daughter phase embedded in the matrix of the mother phase. A more detailed description of the phase diagram can be found in [72].

B. The zone

In a recent paper [72], we reported the numerical solution of Eq. (31) describing the motionless and the propagating crack-process zone complex. By focusing on the results [72] with $V = 0$, one obtains the case of the motionless crack-zone ensemble, which we address in this paper. Let us recite a few results of [72] and [82], which are necessary to follow this paper.

We simulated (31) within domain IV of the phase diagram shown in Fig. 3. The details of the simulation are described in Appendix A. All simulations were performed with $b = 1$. In this case, the upper spinodal is $a_{\text{up}} = 1/4$, while the binodal is $a_b = 3/16 \approx 0.18$. For the simulation, we selected six values of the parameter $a = 0.20 + 0.01 \times i$, ($i = 0, 1, \dots, 5$) taken between these boundaries. They are shown in Fig. 3 by diamond, asterisk, disk, filled square, triangle, and open square correspondingly.

The simulation returns the distributions $u = u(x, y)$ at the values of a , which were listed earlier. Figure 4(a) shows a typical distribution $u(x, y)$ at $a = 0.24$, $b = 1$. Because of the mirror symmetry, we only display the distribution at $y \geq 0$. The solid line at $x \leq 0$, $y = 0$ (arrow) indicates the crack's position concerning the order parameter distribution with its tip in the point $x = y = 0$.

Figure 4(b) shows the zone boundary of the distribution shown in Fig. 4(a). The zone boundary closely resembles the shape of the cardioid. It exhibits, however, a small but essential difference from the cardioid configuration. Indeed, Fig. 4(c) displays a blown-up view of a portion of the boundary behind the crack tip. One observes that the boundary does not hit the crack surface exactly at the crack tip, as it would in the cardioid case. Instead, it meets the crack surface at a distance l behind the tip. For instance, in the case $a = 0.24$ shown in Fig. 4(c) we found l to be about 18 dimensionless units. The distributions at other a values ($a = 0.20, 0.21, 0.22, 0.23$, and 0.25) are similar in their shapes to that shown in Fig. 4. These distributions only differ from one another by their sizes. The most important geometric parameters, the zone width τ and contact length l (see Fig. 1), illustrating the dependence of the zone sizes on the parameter a are displayed in Figs. 5(a) and 5(b). The dots show the simulation results.

One can see that τ grows from about 500 dimensionless units at $a = 0.25$ to 12 718 units at $a = 0.20$. Meanwhile, at the same a values the contact length l increases from 15.1 to 132.4 units.

The zone interface surface tension is described by the term $g(\nabla\eta)^2/2$ in the free energy density $\Phi_{\text{ph}}(4)$ transforming into

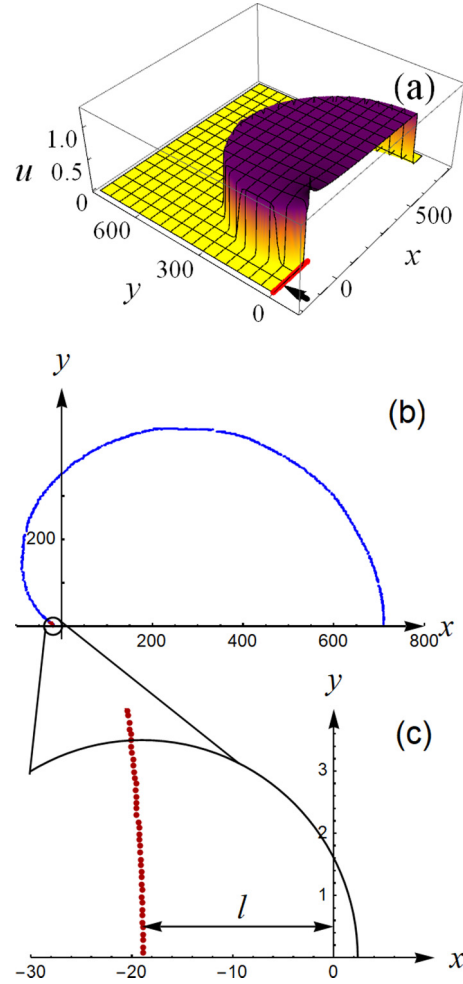


FIG. 4. (a) Dimensionless order parameter $u = u(x, y)$ at $a = 0.24$ and $b = 1$. Only the part at $y \geq 0$ is displayed. The red solid line (pointed out by the arrow) indicates the crack position. (b) The boundary of the zone shown in (a) in the (x, y) plane. (c) Its fragment (shown in red) in the vicinity of the x axis enclosed in a circle in (b). The zone boundary hits the crack surface at the point $(-18, 0)$ behind the crack tip placed at $(0, 0)$ yielding the contact length $l \approx 18$.

$\Phi_s = (\nabla u)^2/2$ in terms of the dimensionless variables. In [71], we derived the expression for the surface energy in terms of the interface boundary curvature radius R_c . In dimensionless variables, it takes the following form:

$$\Phi_s = \frac{a^{1/2} u_d^2}{R_c} \quad (36)$$

where u_d represents the solution of (31) with $\Delta u \equiv 0$ and $U(x, y) = 0$ [72]:

$$u_d = \sqrt{\frac{b + (b^2 - 4a)^{1/2}}{2}}. \quad (37)$$

The boundary curvature radius in front of the tip is about the zone width: $R_c \sim \tau$. Furthermore, in Fig. 5(a) one can see that $\tau \gg 1$. Therefore, we neglect Φ_s when describing the zone size in front of the crack tip. The zone boundary condition then reduces to that of the local binodal, that is $a - \sqrt{2} \cos(\theta/2) r^{-1/2} = 3b^2/16$ yielding the cardioid $r(\theta) =$

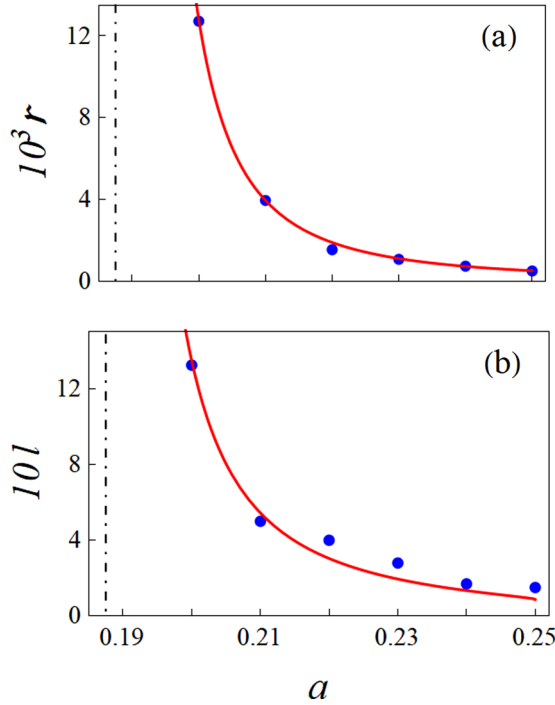


FIG. 5. The zone width r (a) and contact length l (b) as functions of a . In both cases, the dots show the values obtained by simulations at $b = 1$ and different a values. The solid line in (a) corresponds to the approximate relation (38), and in (b) to (39) with $l_0 \approx 10.42$. The dot-dashed vertical line indicates the binodal position where both curves diverge.

$\tau \cos^2(\theta/2)$ with

$$\tau \approx \frac{2}{(a - 3b^2/16)^2}. \quad (38)$$

The run of the curve (38) as a function of a is shown in Fig. 5(a) by the solid line.

The setback observed in all of our simulations arises because of the surface tension of the zone boundary. The latter only plays an essential role in the vicinity of the point $x = y = 0$. Here it makes the cusp-shaped configuration of the cardioid energetically unfavorable forcing the boundary to take a smooth configuration. One can approximate it by a portion of a circle with a radius equal to the curvature radius of the invagination [82], as we describe in detail in Appendix B. This yields the dimensionless contact length l expressed in terms of a and b :

$$l \approx \frac{l_0}{16a - 3b^2} \frac{[b(b^2 - 4a)^{1/2} - 2a + b^2]^{1/4}}{[8a - b^2 - b(b^2 - 4a)^{1/2}]^{1/2}} \quad (39)$$

with $l_0 \approx 10.42$. Its behavior at $0.20 \leq a \leq 0.25$ and $b = 1$ is shown by the solid line in Fig. 5(b).

One sees that the contact length l diverges as it approaches to the binodal $a \rightarrow a_b$ (35) as $l \sim (a - a_b)^{-1}$, and takes a finite value $l_{up} \approx 8.76b^{-5/4}$ at the upper spinodal $a = a_{up}$ (34). The latter diverges at the tricritical point $b = 0$ of the phase diagram.

This setback plays an essential role in forming the transformation toughness, as we prove below.

VI. EFFECTIVE STRESS INTENSITY FACTOR

Using these results let us turn to the calculation of the perturbation of the stress intensity factor according to Bueckner's algorithm.

A. Within the Green function approach

1. Step 1

During the first step, one defines a first stressed state in a hypothetical crack-free body, which, nevertheless, contains the process zone. This step is performed by using the Green function. It is straightforward to use it in the form of the stress in the point $z = x + iy$ generated by the local force $f_x + if_y$ applied in the point $Z = X + iY$ derived in [100]. Here i is the imaginary unit. The expression reads

$$\Phi(z) = \frac{f_x + if_y}{8\pi(1-\nu)} \frac{1}{z - Z}, \quad \Psi(z) = \frac{k(f_x - if_y)}{8\pi(1-\nu)} \frac{1}{z - Z} - \frac{\bar{Z}(f_x + if_y)}{8\pi(1-\nu)} \frac{1}{(z - Z)^2}. \quad (40)$$

Here $\Phi(z)$ and $\Psi(z)$ are Kolosov-Mushelishvili potentials, the bar over the symbol [like \bar{Z} , or $\bar{\Phi}'(z)$] means its complex conjugation: $\bar{Z} = X - iY$, and $k = 3 - 4\nu$. Let us stress that in this section all the coordinates x, y, z, X, Y , and Z are dimensional. They have the usual dimension of length. The stress in the point z can be defined using the standard relation of the plane theory of elasticity [99]:

$$\sigma_{yy} = \text{Re}[2\Phi(z) + z\bar{\Phi}'(z) + \Psi(z)]. \quad (41)$$

By passing to the point lying on the crack contour $z = x$ ($x < 0, y = 0$) and integrating over the domain Ω one finds the stress $\sigma_{yy}(x)$ of the first stressed state. For compactness, we represent it in the form of two terms: $\sigma_{yy}(x) = \sigma_{yy}^{(1)}(x) + \sigma_{yy}^{(2)}(x)$, where

$$\sigma_{yy}^{(1)}(x) = -\frac{A}{4\pi(1-\nu)} \times \iint_{\Omega} \left\{ \frac{(X-x)[(1+2\nu)Y^2 - (1-2\nu)(X-x)^2]}{[(X-x)^2 + Y^2]^2} \times \frac{\partial \eta^2(X, Y)}{\partial X} \right\} dXdY, \quad (42)$$

$$\sigma_{yy}^{(2)}(x) = -\frac{A}{4\pi(1-\nu)} \times \iint_{\Omega} \left\{ \frac{Y[(3-2\nu)Y^2 + (1-2\nu)(X-x)^2]}{[(X-x)^2 + Y^2]^2} \times \frac{\partial \eta^2(X, Y)}{\partial Y} \right\} dXdY. \quad (43)$$

These expressions enable us to pass to the second step of Bueckner's algorithm.

2. Step 2

Within this step, one uses the first stressed state to obtain the perturbation of the stress intensity factor, δK_I :

$$\delta K_I = -\sqrt{\frac{2}{\pi}} \int_0^\infty \frac{\sigma_{yy}(-x)}{\sqrt{x}} dx. \quad (44)$$

Let us now pass from the dimensional order parameter and coordinates x , X , and Y with the dimension of length to dimensionless parameters u , ξ , x' , and y' :

$$\eta(X, Y) = \eta_0 u(x', y'), \quad x = -R_0 \xi, \quad X = R_0 x', \quad Y = R_0 y' \quad (45)$$

where the factors η_0 and R_0 are determined by (30).

Using (42) and (43) one writes down the perturbation δK_I as follows:

$$\delta K_I = -A\eta_0^2 R_0^{1/2} \zeta_0. \quad (46)$$

The dimensionless parameter ζ_0 is equal to an integral expressed in terms of the dimensionless variables ξ , x' , and y' :

$$\zeta_0 = \int_0^\infty \frac{d\xi}{\sqrt{\xi}} \iint_{\Omega} dx' dy' \left\{ P_1(\xi, x', y') \frac{\partial u^2(x', y')}{\partial x'} + P_2(\xi, x', y') \frac{\partial u^2(x', y')}{\partial y'} \right\} \quad (47)$$

with

$$P_1(\xi, x', y') = -\frac{(x' + \xi)[y'^2(1 + 2\nu) - (x' + \xi)^2(1 - 2\nu)]}{(2\pi)^{3/2}(1 - \nu)[(x' + \xi)^2 + y'^2]^2} \quad (48)$$

and

$$P_2(\xi, x', y') = -\frac{y'[y'^2(3 - 2\nu) + (x' + \xi)^2(1 - 2\nu)]}{(2\pi)^{3/2}(1 - \nu)[(x' + \xi)^2 + y'^2]^2}. \quad (49)$$

One finds the perturbed stress intensity factor K_I in terms of $K_I^{(\text{ap})}$ that was originally applied to the crack:

$$K_I = K_I^{(\text{ap})} - A\eta_0^2 R_0^{1/2} \zeta_0. \quad (50)$$

Therefore, the problem reduces to the calculation of the single parameter ζ_0 (47). Below, we estimate the integral (47) numerically. After obtaining ζ_0 , one determines the effective stress intensity factor K_I using (50) and, with its use, finds the fracture toughness. We fulfill this program later on in the present paper.

Let us note, however, that the numerical estimation of the integral according to (47)–(49) is prone to numerical errors. They are partly due to the singular character of the expressions for $P_1(\xi, x', y')$ and $P_2(\xi, x', y')$. The determination of the derivatives $\partial u^2(x', y')/\partial x'$ and $\partial u^2(x', y')/\partial y'$ from the numerical data for $u(x', y')$ also introduces errors. For the sake of control, in parallel to the Green function method, we also apply the method based on the weight functions, which will be described in the next section.

B. The weight functions procedure

The weight functions method that was introduced by Bueckner [101] has been applied by McMeeking and Evans to define the perturbation of the stress intensity factor by the process zone and the zone-wake complex within the mechanical approach [48]. Here, we adopt this procedure for the field-theoretical approach.

The weight functions method expresses the perturbation of the stress intensity factor as follows:

$$\delta K_I = p_1 \oint_{\mathcal{C}} (\mathbf{H} \cdot \mathbf{n}) dS \quad (51)$$

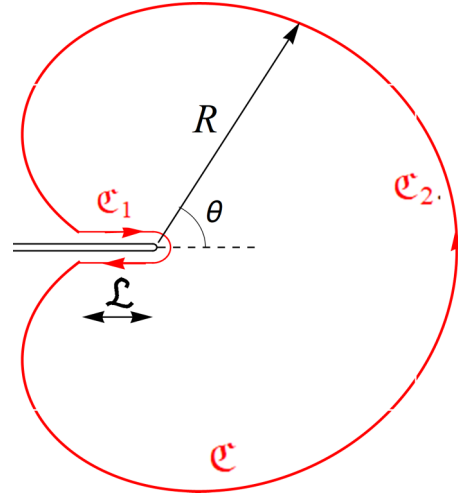


FIG. 6. Contour \mathcal{C} of integration of (51) consisting of two subcontours, \mathcal{C}_1 along the crack and \mathcal{C}_2 along the zone boundary with the mother phase described by $R = R(\theta)$. The contact length \mathcal{L} where the zone meets the crack surfaces is indicated.

where p_1 is the normal stress at the zone boundary [48]. In terms of the order parameter one expresses it as $p_1 = A\eta^2$.

By adopting the weight function procedure to the field-theoretical approach, we need to approximate the order parameter distribution $\eta = \eta(R)$ by a step function. Let us approximately assume it to be strictly zero outside of the zone. Inside, we take a constant value from the solution of a homogeneous problem [72]:

$$\eta = \eta_0 u_d \quad (52)$$

where u_d is given by the expression (37).

The integral (51) runs along the closed contour $\mathcal{C} = \mathcal{C}_1 \cup \mathcal{C}_2$. The contour \mathcal{C}_1 goes along the line where the zone contacts both crack surfaces, with the length \mathcal{L} (referred to as the *dimensional contact length* with the dimension of meter). The contour \mathcal{C}_2 runs along the zone boundary with the mother phase and can be characterized by the radius vector $R = R(\theta)$, as one can see in Fig. 6. Let us again pass from \mathcal{L} and R with the dimensions of length to the dimensionless variables l and r :

$$\mathcal{L} = R_0 l, \quad R(\theta) = R_0 r(\theta). \quad (53)$$

In terms of the dimensionless variables l and $r(\theta)$, one can express the weight functions vector \mathbf{H} , the normal unit vector \mathbf{n} , and the arc element dS along \mathcal{C}_2 as follows:

$$\mathbf{H} = \frac{1}{2\sqrt{2}\pi(1 - \nu)R_0^{1/2}\sqrt{r(\theta)}} (h_1, h_2) \quad (54)$$

where

$$h_i = \begin{cases} \cos(\theta/2)[2\nu + \sin(\theta/2)\sin(3\theta/2)], & i = 1 \\ \sin(\theta/2)[-2\nu - \cos(\theta/2)\cos(3\theta/2)], & i = 2 \end{cases}$$

and

$$\mathbf{n} = \left(\frac{\sin(\theta)r'(\theta) + \cos(\theta)r(\theta)}{\sqrt{r'^2(\theta) + r^2(\theta)}}, -\frac{\cos(\theta)r'(\theta) - \sin(\theta)r(\theta)}{\sqrt{r'^2(\theta) + r^2(\theta)}} \right) \quad (55)$$

and

$$dS = R_0 \sqrt{r'^2(\theta) + r^2(\theta)} d\theta. \quad (56)$$

Let us represent δK_I as a sum $\delta K_I = \delta K_I^{(1)} + \delta K_I^{(2)}$ corresponding to the portions \mathcal{C}_1 and \mathcal{C}_2 of the contour \mathcal{C} . One can calculate the first contribution straightforwardly:

$$\delta K_I^{(1)} = -\frac{4A\eta_0^2 R_0^{1/2} u_d^2}{\sqrt{2\pi}} \sqrt{l}. \quad (57)$$

The second contribution takes the form

$$\delta K_I^{(2)} = \frac{A\eta_0^2 R_0^{1/2} u_d^2}{2\sqrt{2\pi}(1-\nu)} I \quad (58)$$

where I is the integral along the contour \mathcal{C}_2 :

$$I = \frac{1}{2\sqrt{2\pi}(1-\nu)} \int_0^\pi \{r'(\theta)J_1(\theta) + r(\theta)J_2(\theta)\} \frac{d\theta}{\sqrt{r(\theta)}} \quad (59)$$

where

$$J_i(\theta) = \begin{cases} \sin(\theta/2)[(5-8\nu)\cos(\theta) - 4\nu + 1], & i = 1 \\ \cos(\theta/2)[(7-8\nu)\cos(\theta) + 4\nu - 5], & i = 2. \end{cases}$$

By collecting these results together one comes to the expression (46) with

$$\zeta_0 = \zeta_1 + \zeta_2, \quad \zeta_1 = \frac{2^{3/2} u_d^2}{\pi^{1/2}} \sqrt{l}, \quad \zeta_2 = -\frac{u_d^2 I}{\pi \sqrt{2}(1-\nu)}. \quad (60)$$

As soon as the contour \mathcal{C}_2 has been obtained, the dimensionless parameter ζ_0 can be calculated.

The dimensionless parameter ζ_0 determines the magnitude of the zone effect on the fracture toughness. Therefore, it is essential to find its absolute value. We do this numerically in the following section.

C. The value of ζ_0

1. Numerical results

The details of the numerical estimation of integrals (47) and (59) are given in Appendix A. These procedures enabled us to find $\zeta_0 = \zeta_0(a)$, which is displayed in Fig. 7. Dots show the behavior of ζ_0 at various values of a obtained by simulations at $b = 1$ with the help of both the Green function and weight functions methods. Both results are pretty close to one another.

We indicate binodal position $a_b = 3/16$ by the dashed vertical line in Fig. 7. One can see that ζ_0 increases as it approaches the binodal (35).

This result differs from the previous ones. Indeed, within the terminology of this paper, the previous authors [48,49] and others [13] find $\zeta_0 \equiv 0$. Therefore, the fact that ζ_0 is essentially nonzero is a striking result of this paper.

2. The analytical expression for ζ_0

To understand the latter fact, let us first observe that ζ_1 , the first part of ζ_0 expressed by the weight function method (60), is proportional to \sqrt{l} . Here l is the dimensionless contact length that was discussed in Sec. V A. Second, our numerical calculations show that in all cases the ratio ζ_2/ζ_1 is small,

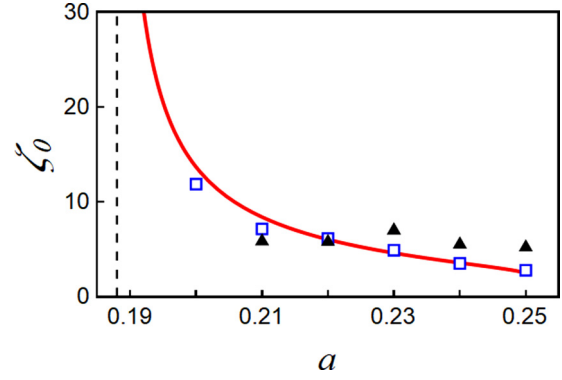


FIG. 7. Dependence of ζ_0 on a at $b = 1$. The filled triangles show the results obtained from the simulation using the Green function method, while the open squares show those calculated within the weight functions approach. The solid line shows the behavior of the analytical function $\zeta_0(a)$ Eq. (61). The dashed line shows the position of the binodal, $a = 3/16$.

close to 0.2. Thus, with reasonable accuracy, one can approximate the ζ_0 as $\zeta_0 \approx \zeta_1/0.8 \sim \sqrt{l}$. Appendix B derives the analytical expression for $l = l(a, b)$ (39).

Using the expressions (60), (52), and (39) one finds

$$\zeta_0 \approx 3.22 \frac{[(b^2 - 4a)^{1/2} + b][b^2 - 2a + b(b^2 - 4a)^{1/2}]^{1/8}}{(16a - 3b^2)[8a - b^2 - b(b^2 - 4a)^{1/2}]^{1/4}}. \quad (61)$$

The solid line in Fig. 7 shows the behavior of ζ_0 (61) at $b = 1$. One can see that it agrees with our numerical results.

Let us now pass from the dimensionless to the original parameters. This is achieved by applying (33) to (61). One finds the expression for ζ_0 in terms of the original material constants:

$$\zeta_0 \approx 3.28 \left[\frac{A(1-2\nu)(1+\nu)}{Eg^{1/4}} K_I \right]^{1/6} \left(\frac{\gamma}{\beta^2} \right)^{1/8} s \left(\frac{\alpha\gamma}{\beta^2} \right) \quad (62)$$

where for the sake of shortness, we introduced the dimensionless variable $s = s(\lambda)$:

$$s(\lambda) = \frac{[1 + (1 - 4\lambda)^{1/2}][1 + (1 - 4\lambda)^{1/2} - 2\lambda]^{1/8}}{(16\lambda - 3)^{1/2}[8\lambda - 1 - (1 - 4\lambda)^{1/2}]^{1/4}} \quad (63)$$

with $\lambda = \alpha\gamma/\beta^2$.

The expression (62) is defined at $\alpha_b < \alpha \leq \alpha_{up}$, that is, below the upper spinodal α_{up} but above the binodal α_b . We now express the latter in terms of the dimensional parameters α , β , and γ as $\alpha_{up} = \beta^2/4\gamma$ and $\alpha_b = 3\beta^2/16\gamma$.

The factor s only depends on the dimensionless combination $\lambda = \alpha\gamma/\beta^2$, and thus, on the position in the phase diagram defined within the interval:

$$\frac{3}{16} < \frac{\alpha\gamma}{\beta^2} \leq \frac{1}{4}.$$

$s(\lambda)$ varies from its minimum value $s_{min} \approx 2.59$ at the upper spinodal $\alpha_{up}\gamma/\beta^2 = 1/4$ to infinity at the binodal $\alpha_b\gamma/\beta^2 = 3/16$.

Figure 8 displays its behavior.

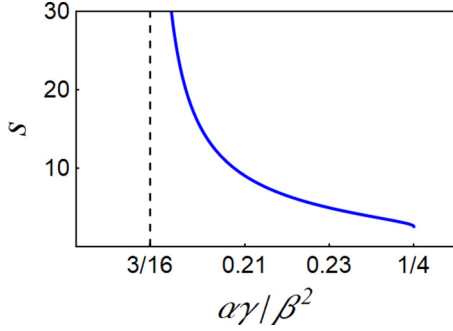


FIG. 8. Behavior of the dimensionless factor s depending on the dimensionless combination of the Landau potential coefficients $\alpha\gamma/\beta^2$. The dashed vertical line indicates the binodal position.

By introducing the binodal temperature T_b as $\alpha_0(T_b - T_c) = 3\beta^2/16\gamma$, one expresses λ as

$$\lambda = \frac{3}{16} \frac{T - T_c}{T_b - T_c} \quad (64)$$

showing that $s = s[(T - T_c)/(T_b - T_c)]$ depends on the proximity of the solid to the Curie temperature T_c .

Close to the binodal $\alpha_b = 3\beta^2/16\gamma$ the expression ζ_0 (62) simplifies as follows:

$$\zeta_0 \approx 5.37 \frac{|\beta|^{5/4} \gamma^{1/8}}{(16\alpha\gamma - 3\beta^2)^{3/4}} \left[\frac{A(1-2\nu)(1+\nu)}{Eg^{1/4}} \right]^{1/6} K_I^{1/6}. \quad (65)$$

One sees that ζ_0 diverges in the vicinity of the binodal α_b as $\zeta_0 \sim (16\alpha\gamma - 3\beta^2)^{-3/4}$ as can be seen in Fig. 7.

If a tricritical point $\beta = 0$ exists in the phase diagram, ζ_0 diverges in its vicinity as $\zeta_0 \sim \beta^{-1/4}$.

Its smallest value

$$\zeta_0^{(\text{up})} \approx 3.01 \left(\frac{\gamma}{\beta^2} \right)^{1/8} \left[\frac{A(1-2\nu)(1+\nu)}{Eg^{1/4}} \right]^{1/6} K_I^{1/6} \quad (66)$$

parameter ζ_0 achieves at the upper spinodal α_{up} .

VII. TRANSFORMATION TOUGHNESS

A. The analytical expression for the fracture toughness

The fracture toughness K_{IC} is formed by interatomic interactions and it is directly related to the height V_0 of the atoms' potential barrier. One can estimate it as $V_0 \sim \Gamma a_0^2$, where Γ is the fracture energy, while a_0 is the atomic size. In lattices with a few atoms per unit cell, a_0 has the same order of magnitude as the lattice constant.

During the phase transformation, the atoms displace from their positions in the mother phase. One can interpret this as the action of a molecular force $\phi = \phi(\eta)$ exerted on the atoms. It is balanced by the elasticity resulting in the transformation strain ε_0 . One can, therefore, estimate it as $\phi \sim \varepsilon_0 E a_0^2$. As soon as a bond breaks, the atom displaces approximately over a_0 . Thus, the work of the force ϕ in the process of the bond breaking can be estimated as $\Delta V_0 \sim \phi a_0$. This work yields the estimate of the decrease of the barrier height $\Delta V_0 \sim \varepsilon_0 E a_0^3$. One finds

$$\frac{\Delta V_0}{V_0} \sim \frac{\varepsilon_0 E a_0}{\Gamma}.$$

Taking typical values $\varepsilon_0 \sim 10^{-3}$, $E \sim 10^{11}$ Pa, $a_0 \approx 3 \text{ \AA}$, and $\Gamma \sim 10$ to 10^2 J/m² one finds $\Delta V_0/V_0 \sim 10^{-3}$ to 10^{-4} , which suggests that the perturbation of the potential barrier height due to the phase transformation is typically small.

The potential barrier V_0 determines the fracture toughness K_{IC} measured deep in the mother phase, where no transformational process zone exists. Since $\Delta V_0/V_0 \ll 1$ one regards the mother-phase fracture toughness K_{IC} as a material constant characterizing the solid.

In the course of a fracture experiment, however, one does not measure this material constant directly. In contrast, one measures the value of the stress intensity factor $K_I^{(\text{ap})}$ applied to the solid. Depending on the character of the experiment, one then relates it to the fracture toughness. Let us denote this fracture toughness value $K_{IC}^{(\text{m})}$, where ‘‘m’’ represents ‘‘measured.’’ It is this measured fracture toughness $K_{IC}^{(\text{m})}$ that exhibits an increase as soon as the process zone arises.

The crack starts propagating as soon as the perturbed stress intensity factor K_I (15) becomes equal to the material constant K_{IC} . Therefore, by replacing in (50) $K_I \rightarrow K_{IC}$ and $K_I^{(\text{ap})} \rightarrow K_{IC}^{(\text{m})}$ one obtains the measured fracture toughness in terms of the material constant K_{IC} and ζ_0 :

$$K_{IC}^{(\text{m})} = K_{IC} + A\eta_0^2 R_0^{1/2} \zeta_0. \quad (67)$$

Making use of the analytical relation (62) for ζ_0 , one finds the analytical expression for $K_{IC}^{(\text{m})}$:

$$K_{IC}^{(\text{m})} = K_{IC} + 3.41s \left(\frac{\alpha\gamma}{\beta^2} \right) [(1-2\nu)(1+\nu)]^{1/2} \times \left(\frac{A^{12}g}{\beta^2\gamma^3} \right)^{1/8} \sqrt{\frac{K_{IC}}{E}}. \quad (68)$$

The second term in (68) describes the intensity of the zone impact on the fracture toughness.

B. Relative perturbation of the fracture toughness

We obtained the analytical expression (68) for the transformation toughness. The relative perturbation of the fracture toughness $(K_{IC}^{(\text{m})} - K_{IC})/K_{IC}$ takes the following form:

$$\frac{K_{IC}^{(\text{m})} - K_{IC}}{K_{IC}} = s \left(\frac{\alpha\gamma}{\beta^2} \right) \Delta \quad (69)$$

where

$$\Delta = 3.41 \left[\frac{(1-2\nu)(1+\nu)}{K_{IC}E} \right]^{1/2} \left(\frac{A^{12}g}{\beta^2\gamma^3} \right)^{1/8}. \quad (70)$$

In this product s only depends on the position in the phase diagram, while Δ depends on the values of the material constants. In a given phase diagram point, the factor Δ (70) determines the absolute value of the fracture toughness perturbation. It is, thus, essential to estimate it. This question will be addressed in Discussion in Sec. VIII F.

VIII. DISCUSSION

A. The order parameter in the Landau theory

1. The order parameter definition

It is essential to specify the order parameter's physical origin since, in various scientific fields, its definitions quali-

tatively differ from one another. In this paper, we regard the process zone as the phase transformation localized at the crack tip. Furthermore, we only consider the cases in which the symmetry group of the crystal in the matrix, \mathcal{G} , is connected by the group-subgroup relation to the groups \mathcal{G}_i ($i = 1, 2, \dots$) of the daughter phases: $\mathcal{G}_i \subset \mathcal{G}$. In this case, one describes the matrix-zone transformation within the Landau theory of phase transitions [74,90,92].

In the case of the structural phase transitions (which we only consider here), the phase transformation occurs due to the crystal lattice's structural instability. It forms a new lattice structure in which some atoms displace from their former positions (in the case of the displacive phase transformations) or redistribute over a set of available positions (in the order-disorder ones). In both cases, one characterizes the transition by a set of degrees of freedom of the lattice involved in forming the new structure.

In the Landau theory, the order parameter $\eta = (\eta_1, \eta_2, \dots, \eta_n)$ is the set of such degrees of freedom [92].

2. How one determines the order parameter in practice

For a given group \mathcal{G} , the choice of the order parameter η fixes all possible subgroups $\mathcal{G}_i \subset \mathcal{G}$ ($i = 1, 2, \dots$) of the daughter phases. The latter observation yields a practical way to determine the order parameter. Namely, one scans all possible order parameter candidates and finds one such that its nonzero components decrease the mother-phase symmetry \mathcal{G} down to the known experimentally established subgroups \mathcal{G}_i .

Let us give an example. In BaTiO₃, one observes the phase transitions from the cubic mother phase with the symmetry group $\mathcal{G} = Pm\bar{3}m$ (O_h^1) to its subgroups. Here we give the symmetry both in the International and Schoenflies notations. The transition is described by the three-component order parameter $\eta = (\eta_1, \eta_2, \eta_3)$ representing a three-dimensional (3D) vector in the BaTiO₃ case. In the mother phase, $\eta_1 = \eta_2 = \eta_3 = 0$ corresponding to the group \mathcal{G} .

In the daughter phases, some of its components become nonzero. Depending upon its orientation concerning the cube, the vector $\eta \neq 0$ decreases the cubic symmetry. For instance, the tetragonal daughter phase $\mathcal{G}_1 = P4mm$ (C_{4v}^1) is described by $\eta_3 \neq 0, \eta_1 = \eta_2 = 0$. The rhombohedral daughter phase $\mathcal{G}_2 = R3m$ (C_{3v}^5) one obtains with $\eta_1 = \eta_2 = \eta_3 \neq 0$, and the orthorhombic daughter phase $\mathcal{G}_3 = Amm2$ (C_{2v}^{14}) one obtains with $\eta_1 = \eta_2 \neq 0, \eta_3 = 0$ [102].

In general, the determination of the order parameter is a complex crystallographic problem. Its detailed description is out of the scope of our paper. We refer the readers to such books as [90,92,93].

3. One-component versus multicomponent order parameter

In this paper, we only studied the case of a one-component order parameter. There are many materials exhibiting phase transformations described by the one-component order parameter such as anisotropic magnetics, like K₂CoF₄, Rb₂CoF₄, and others [103]; uniaxial ferroelectrics, such as LiTaO₃, LiNbO₃, K₂PO₄, Pb₅GeO₁₁, triglycine sulfate (NH₂CH₂COOH)₃H₂SO₄, and SbSJ [104]; and binary bcc alloys, such as Fe-Be [105] and CuZn [74]. The one-component

order parameter describes the α - β transition in quartz [106] and the transition from the normal into the superconductive phase in Sn, Pb, Fe, and most other superconductive materials [107]. In such cases, our approach is directly applicable.

In many cases, it can also be applied to zones described by multicomponent order parameters. Indeed, many transitions controlled by $\eta = (\eta_1, \eta_2, \dots, \eta_n)$ exhibit one-parametric low-symmetry phases. These are the phases in which only one order parameter component is unequal to zero, such as $(\eta, 0, \dots, 0)$ or $(0, \eta, \dots, 0)$, and those exhibiting several nonzero components, which are, however, equal to one another, such as $(\eta, \eta, 0, \dots, 0)$ or $(\eta, \eta, \dots, \eta)$, and alike. We have seen an example of such a case for the phases $\mathcal{G}_1, \mathcal{G}_2$, and \mathcal{G}_3 in BaTiO₃. This paper also directly applies to such one-parametric phases, provided that the order parameter only couples with the diagonal components of the strain tensor.

One can also face multiparametric phases. In these cases, the combinations of the order parameter components such as $(\eta_1, \eta_2, 0, \dots, 0)$ or $(\eta_1, \eta_2, \eta_3, 0, \dots, 0)$ or $(\eta_1, \eta_2, \dots, \eta_n)$ with $\eta_1 \neq \eta_2 \neq \dots \neq \eta_n$ describe various daughter phases or domains (twins, variants). In such a situation, one cannot automatically use the results that we have reported here but needs to solve the equation of state [like Eq. (8)] for all components of the order parameters simultaneously. However, this problem is out of the scope of the present paper.

Finally, some symmetries allow the order parameter to interact with the deviatoric components of the strain in addition to the dilatation. An example of such a study one finds in [88]. In that case, the situation becomes more complicated because the zone may have a complex structure comprising different phases and domains (twins, variants), as in the case of fracture of ferroelectrics [108]. The zone configuration also becomes more intricate. Such a problem requires an independent analysis. In such cases, we expect the results to differ from the predictions of this paper.

4. Landau order parameter versus the phase field one

The popular phase-field method also uses the term "order parameter" [109]. In this method, one determines the order parameter as an indicator function, often a scalar one, to distinguish different states of the materials during the simulation. The advantage of such an approach is its flexibility enabling one to conveniently account for qualitatively different states of the solids possibly containing a crack [110]. The same flexibility generates difficulties to define the order parameter field such that its relation to the material parameters would be unique and physically grounded [111].

In the Landau theory, one should regard parameters of the Landau potential (such as $g, \alpha_0, \beta, \gamma$, and A) as the material constants of the crystal. Using modern methods, they have been measured for many materials (see, for example, [112,113]).

Formally, however, Landau's theory of phase transitions and the phase-field approach similarly treat the order parameter. Indeed, in both cases, one builds the free energy functional in terms of the order parameter and further uses it to derive its equation of state (or motion) according to the standard rules. The latter makes it possible to combine the phase-field method

with the Landau theory within the same numerical study, as was recently reported in [88].

B. The case of a higher order Landau polynomial

The expressions (68), (76), and (77) that follow use the dependence of $K_{IC}^{(m)}$ on β and γ which suggests that the sixth-order Landau potential can describe the phase transition. For different reasons, the accurate description of the phase transformation and the phase diagram may sometimes require us to account for the order parameter's higher-order terms. On the one hand, even the Landau potential that depends on the one-component order parameter may have more than three minima, thus exhibiting isostructural transformations. On the other hand, the configuration of the Landau potential may occur slightly different from the one described by the sixth-order polynomial, as, for instance, in the BaTiO₃ case [112], and thus one needs to account for higher order terms for its accurate description.

In this latter case, the description of the fracture toughness with the potential (4) still holds as an approximation, and the estimates (76) and (77) given below are still approximately valid.

With these considerations in mind, our estimates can be applied to many (though not all) process zones.

C. Limitations of our approach

Let us briefly list limitations of our approach.

First, we used the linear elastic theory with the free energy (3), squared in terms of the strain. This excludes essentially elastically nonlinear materials from the consideration, such as ferroelastics [94], many martensitic transformations, stishovite [114], and brittle polyacrylamide gels [95].

The second limitation is related to the assumption that the symmetries of the mother and daughter phases are subjected to the group-subgroup relation. This rules out the so-called reconstructive phase transformations in which such a relation does not hold. Let us mention that our theory can be generalized for the reconstructive transformations by using the approach formulated in [115]. This is, however, outside the scope of the present paper.

D. Some generalizations

We demonstrated that the surface tension of the zone boundary itself gives rise to transformation toughness. We did this within the simplified example of the elastically isotropic crystal with the process zone described by a one-component order parameter. Let us now briefly discuss less restricted cases.

Elastically isotropic versus elastically anisotropic single crystal

Although we only addressed the elastically isotropic single crystal for the sake of simplicity, the results qualitatively also hold for weakly anisotropic crystals, such as most cubic metals [116]. However, in strongly elastically anisotropic materials, the curved interface, such as the one shown in Fig. 1, is energetically unfavorable. In such crystals, one expects the zone boundary to consist of plane facets that are separated

from one another by either misfit dislocations or the so-called complexions [117].

E. Relationship to previous results

1. The process zone boundary criterion

The mechanical approach used the plasticitylike criterion to define the process zone boundary in [48–50,52] and other papers [13]. The criteria of plasticity are closely related to the properties of dislocations and other plastic defects. Their generation or propagation starts upon exceeding some critical value of the shear stress or some invariant combination of the stress tensor components [118].

In the inhomogeneous solid, the phase boundary criterion is more complex depending on the stress field's interplay, transformation strain, and the boundary surface tension. Therefore, the criteria used in [13,48–50,52] do not correctly describe the phase boundary. Roitburd and Grinfel'd [70] derived a criterion for a sharp, coherent phase boundary in crystals. We implemented the account for the boundary surface tension in [71] within the Roitburd-Grinfel'd approach. Though sometimes useful, their approach [70,71] leads to a complex integral equation on the phase boundary configuration. In general, this equation is hardly treatable and its use is difficult.

Let us note that the zone boundaries of monocrystals, ceramics, and composites are substantially different.

In ceramics, the zone boundary forms by the stress field, consisting of the stress generated by the crack tip and those generated by the confined grains. The latter exhibit random sizes, shapes, and orientations. Therefore, stress exhibits stochasticity depending on the prehistory of the material and influences the zone boundary configuration. Without the information of its prehistory, the latter cannot be found.

In composites, the boundary can lie outside of those grains that exhibit the phase transformation. In this case, the criteria such as those formulated in [70,71] do not directly apply.

In these materials, the choice of the boundary criterion is complicated and is most likely phenomenological.

The field-theoretical approach [68,76–82] solves the problem of the boundary criterion differently: it formulates the process zone problem in terms of the order parameter. The latter originates from a set of the microscopic coordinates of the atoms inherently involved in the phase transformation: that is, their displacements control the variation of crystal structure during the transformation. These coordinates after coarse graining obey the Ginzburg-Landau equation of state (26). The latter also describes the spatial distribution of the intrinsic degrees of freedom of the solid in the inhomogeneous spatial environment. Let us note that the field-theoretical approach automatically accounts for the zone boundary surface tension due to the term $\sim g(\nabla\eta)^2$ in (4).

Within this approach, the solution $\eta(\mathbf{R})$ exhibits a kink, and one describes the zone boundary as the kink configuration. An example of such a kink and its configuration can be seen in Figs. 4(a) and 4(b), and in multiple images of [72].

Within the model developed in this paper, it is the surface tension that gives rise to the zone setback and, thus, to the transformation toughness. Consequently, one observes that $(K_{IC}^{(m)} - K_{IC})/K_{IC} \sim g^{1/8}$ (69). In addition to single crystals,

our results can be applied to polycrystals and crystals with mosaic structure, provided that the zone size \mathfrak{R} is smaller or comparable to the characteristic dimension of the crystallite d . In the opposite limit $\mathfrak{R} \gg d$, the crystal exhibits the features of ceramics.

2. Coincidence of the mechanical and field-theoretical approaches

In some materials (referred to as those with *manifested first-order transition*), the order parameter exhibits a strong discontinuity in the transition point, the order parameter jump being close to its saturated value η_s . The dependence $\eta = \eta(T)$ closely resembles a step function: $\eta \approx \eta_s$ at $(T \leq T_b)$ and $\eta = 0$ at $(T > T_b)$. In such cases, the use of the Landau theory of phase transitions (if still applicable) brings no advantage to the theory. One can instead exhaustively characterize the transition by the discontinuity η_s in the binodal point T_b or, equally, by the transformation strain ε_0 . The next important characteristic determining the zone is the criterion of its phase boundary. If the latter accounts for the zone surface tension, the mechanical and field-theoretical approaches coincide.

3. Irreversibility of the phase transformation

(a) *Irreversibility due to long characteristic time.* In the papers [2,27,28,30,48–50,52] and many others [13] the phase transformation into the metastable daughter phase was assumed to be irreversible. Let us note that the metastable daughter phase corresponds to the less pronounced minimum of the free energy than the mother phase. Therefore, the metastable phase is always out of equilibrium. In equilibrium, the daughter phase vanishes and, in principle, the transformation is always reversible.

However, one can indicate at least two mechanisms making the daughter to mother transformation irreversible from the practical point of view.

The first mechanism occurs if the daughter to mother transformation is of the so-called order-disorder or reconstructive types when the transition mechanism involves overcoming an energetic barrier. Provided that the barrier considerably exceeds $k_B T$ in the unloaded crystal, the characteristic transformation time τ by far exceeds the time of fracture. In this case, once having arisen, the wake persists for the time $t \sim \tau$. In such cases, the mechanism described in the papers [48,49] applies.

The well-known example of such a case is the reconstructive graphite-diamond transition, where the diamond is metastable under the room conditions [107], although it never transforms into the graphite. Cracking of diamond may give rise to the graphite process zone and the persisting wake, as reported in [119].

However, transitions exhibiting huge characteristic times τ are rare. In the case of the transitions of the order-disorder type, the atoms jump between different minima of the local molecular potential overcoming barriers. The characteristic time may be as short as $\tau \sim 10^{-12}$ s as in Rochelle salt, triglicine sulphate, and KD_2PO_4 . One finds an order of magnitude larger characteristic time $\tau \sim 10^{-11}$ s as in KNO_3 and NaNO_2 . The characteristic time achieves as high a value as $\tau \sim 10^{-7}$ s in the case of $\text{AgNa}(\text{NO}_2)_2$ [120]. These values are,

however, by far not enough to regard such transformations as irreversible.

If the solid exhibits a barrierless transformation of the *displacive* type, its characteristic time is still much shorter, $\tau \sim 10^{-13}$ s, as in BaTiO_3 , $\text{Pb}(\text{Ti}_x\text{Zi}_{1-x})\text{O}_3$, and SrTiO_3 [120].

The reversibility of tetragonal to monoclinic phase transformation in ZrO_2 has been also reported [55] and, therefore, cannot explain the transformation toughness phenomenon in this material.

(b) *Irreversibility due to pinning.* The second mechanism is related to the transformation induced plastic deformation. The zone formation may give rise to considerable shear stress on its boundary. It may rearrange plastic defects, such as dislocations, that already exist in the material as observed in NiTi [121], or the new plastic defects may be generated, as those observed in a nanostructured Fe alloy [122]. After the zone advancement, these plastic defects can pin the daughter phase down, forming an irreversible wake. In this case, the wake is stable rather than metastable: the stress field generated by the pinning objects stabilizes it. This stabilized wake contributes to the fracture toughness. One should expect, however, that the contribution of the pinning defects is comparable to that of the wake. Hence, one must also take the latter into account when determining the transformation toughness. Let us note that such a contribution has never been accounted for within the mechanical approach.

(c) *A quasistatic crack propagation.* The key point of early approaches [27–30] as well as those developed by McMeeking and Evans, Rose, and Budiansky *et al.* [48–50,52–54] was the requirement of a quasistatic crack propagation. The reason for such a requirement was that one could not explain the transformation toughness without the wake. It was hypothesized that the latter emerges following the propagating crack-zone complex. Thus, it was assumed that the crack is not truly motionless but propagating with a negligibly small velocity.

As we discovered in [72] in the reversible cases, during the quasistatic crack propagation, the wake completely melts down. The wake can only form as soon as the crack velocity exceeds a certain value. Thus, the mechanism of the persisting wake following the crack that propagates quasistatically does not apply.

4. Fracture toughness outside of the hysteresis

It is generally accepted that the transformation toughness phenomenon only occurs within the hysteresis region of the phase diagram, where the daughter phase is metastable. It is for this reason that so far its only explanation was the formation of the persistent metastable wake during the quasistatic crack propagation [2,27–30,48–50,52–54].

This paper has demonstrated that the transformation toughness phenomenon exists for a motionless crack due to the zone boundary's surface tension. Provided the process zone occurs at the crack tip, its boundary exhibits the surface tension inside and outside the hysteresis. Let us recall that the bifurcation line (line 4 in Fig. 3) lies above the upper spinodal (line 1 in Fig. 3) on the phase diagram. The transformation toughness phenomenon occurs everywhere between lines 3 and 4 of the phase diagram Fig. 3, in the regions IV and V. Note

that among these two regions, only region IV belongs to the hysteresis.

In this paper, we focused on the first-order transitions. However, in the second-order ones, the transformation toughness phenomenon also occurs due to the surface tension.

5. The resonance phenomenon

At certain conditions, the zone size diverges. This phenomenon discovered by Rose [50] was referred to as a *resonance* [52] and studied in detail by Stump and Budiansky, who argued that the resonance takes place as soon as a parameter $\sim \sigma_T/\sigma_m$ achieves a critical value [52]. Here, σ_m is the stress spur at the zone boundary and σ_T is the transformation stress in the unconstrained solid.

Our approach reveals the physical origin of such a resonance. It takes place as soon as the state of the solid approaches the binodal (35).

F. Estimates of the transformation toughness perturbation

1. General estimates

First, let us observe that as long as Eq. (26) describes the first-order transformation, all of its terms are of the same order of magnitude. Indeed, if some of them are much smaller than the others, they should be neglected. The same statement holds for the potential (4). Thus, one finds the estimate:

$$\alpha_0 \Delta T_h \eta^2 \sim |\beta| \eta^4 \sim \gamma \eta^6 \quad (71)$$

where $\Delta T_h = T_{up} - T_b$ is three-quarters of the hysteresis width, the temperature difference between the upper spinodal and the binodal.

The process zone has its internal scale, R_0 (30):

$$R_0 \sim \left(\frac{gE}{AK_{IC}} \right)^{2/3}. \quad (72)$$

Within the narrow transition region of the kink, the expression $g(\nabla\eta)^2$ also becomes of the same order of magnitude as the terms (71), and one can estimate it as $g(\nabla\eta)^2 \sim g\eta^2/R_0^2$ which yields the following relation:

$$\frac{g\eta^2}{R_0^2} \sim |\beta| \eta^4. \quad (73)$$

One can associate the striction constant A to the slope of the phase transition line $\partial T_b/\partial p$ in the phase diagram, which is known for most materials. Indeed, by using the $T_c(p)$ expression (7) one finds $A \sim -\alpha_0 E (\partial T_c/\partial p)$. If the hysteresis is narrow enough, which is true for most dielectrics [107], one finds $\partial T_c/\partial p \sim \partial T_b/\partial p$ yielding

$$|A| \sim \alpha_0 E \left| \frac{\partial T_b}{\partial p} \right|. \quad (74)$$

The estimate of the transformation strain ε_0 reads

$$\varepsilon_0 \sim \frac{A\eta^2}{E}. \quad (75)$$

Making use of (71)–(75) we find a simple estimate for the parameter Δ :

$$\Delta \sim \frac{E\varepsilon_0}{\Delta T_h} \left| \frac{\partial T_b}{\partial p} \right|. \quad (76)$$

Let us mention here that in this paper we focused on the case $A > 0$ corresponding to $\partial T_b/\partial p < 0$. In this case, the process zone of the daughter phase forms within the matrix of the mother phase above the temperature T_b of the bulk phase transition. Below the bulk phase transition temperature, no zone takes place. If $A < 0$ and, thus, $\partial T_b/\partial p > 0$, the zone of the mother phase forms within the matrix of the daughter phase below the bulk transition line, but no zone exists at $T > T_b$. Further details can be found in [77]. With this in mind, one can apply the estimate (76) in both cases $T_b/\partial p > 0$ and $\partial T_b/\partial p < 0$.

Let us further observe that the product $E\varepsilon_0(\partial T_b/\partial p)$ is the shift of the binodal temperature under the effect of the hydrostatic pressure $p_0 \sim E\varepsilon_0$ equal to the spur of the transformation stress. Let us denote it by $\Delta T_b = E\varepsilon_0(\partial T_b/\partial p)$. Thus,

$$\Delta \sim \frac{\Delta T_b}{\Delta T_h}. \quad (77)$$

2. Numerical estimates

The typical value of the transformation strain during phase transitions is $\varepsilon_0 \sim 10^{-3}$; the typical Young's modulus value is $E \sim 10^{11}$ Pa. The phase transition line $T_b(p)$ on the phase diagram can have any slope. However, its typical value is $\partial T_b/\partial p \sim 1 \div 10$ K/kbar = $10^{-8} \div 10^{-7}$ K/Pa, while the hysteresis width is typically $\Delta T_h \approx 1 \div 10$ K [107]. One finds the estimate $\Delta \sim 0.1$ to 10.

Taking into account that $s \gtrsim 0.92$, such estimates show that the measured fracture toughness $K_{IC}^{(m)}$ can achieve values comparable with the original, K_{IC} as well as considerably exceed it.

IX. SUMMARY

We formulated a self-consistent field-theoretical description of the process zone at the tip of a motionless crack. In this approach, we describe the process zone by the spatial distribution of the order parameter. First, we derived a complete system of equations describing the crack-zone complex. We then rigorously reduce this system to a single Ginzburg-Landau equation that is imposed on the order parameter. The latter equation self-consistently describes the first-order local phase transformation, forming the process zone. Its size and properties depend on the position of the solid in its phase diagram. Furthermore, we derived the effective stress intensity factor exerted on the crack depending on the externally applied load and the stressed state generated by the zone. This expression is controlled by a single dimensionless parameter ζ_0 that we determined in quadratures. We then used the previously reported solution [72] and obtained ζ_0 from simulations. The latter enabled us to obtain the transformation toughness numerically. We finally derived accurate analytical expressions both for ζ_0 and the transformation toughness.

In contrast to the common opinion, our results show that the crack in a crystal does not need to propagate to form the transformation toughness. On the contrary, motionless cracks already exhibit this phenomenon. We revealed that this phenomenon originates from the surface tension of the process zone interface. Our results demonstrate the dependence of

the transformation toughness on the solid's position in its phase diagram: the closer the material is to the binodal, the higher the effect. We show that the transformation toughness's impact is proportional to the slope of the phase transformation line in the phase diagram of the solid and the transformation stress. At the same time, it is inversely proportional to the hysteresis width.

APPENDIX A: DETAILS OF THE NUMERICAL APPROACH

1. Simulation details

We simulated the problem by the relaxation method. We formally introduced an artificial time, τ , referred to as the pseudotime, and assumed that $u = u(x, y, \tau)$. Instead of simulating the static equation (31), we simulated the following pseudo-time-dependent dynamic equation:

$$\frac{\partial u}{\partial \tau} = \Delta u - [a - U(x, y)]u + bu^3 - u^5 \quad (\text{A1})$$

with some initial conditions. It is important that the initial conditions are nonzero: $u(x, y, 0) \neq 0$. At $\tau \rightarrow \infty$ the solution $u(x, y, \infty)$ of (A1) automatically converges to the solution of the static equation (31). Let us note that the closer is the initial condition to the final solution, the faster the process converges.

A detailed discussion on the application of the relaxation method to equations like (31) as well as its pitfalls one finds in [123] and in Appendix B of the paper [72].

We simulated Eq. (A1) using COMSOL 5.5. Most settings of this program coincide with those reported in our previous paper [72] to which we refer the reader for details. The latter paper, however, reports the results obtained with the 5.3 version of COMSOL. Version 5.5 exhibits a handy new feature in the so-called Adaptive Mesh Refinement properties. It enabled us to obtain the solution in the points close to the binodal marked by the diamond and asterisk in Fig. 3.

Indeed, the sizes of the zones studied in [72] were up to $\tau \lesssim 1 \times 10^3$ of the dimensionless units. This sets the domain's size in which the problem is solved to be somewhat larger than τ . The zone interface's width is about a few dimensionless units, as demonstrated in Fig. 12 of the paper [72]. To resolve the zone structure of the interface such that the integrals (47) could be reliably calculated numerically (see the next section), one needs the mesh size of at least ≈ 0.1 unit. The application of a homogeneous mesh with such a mesh size leads to the $\approx 10^8$ degrees of freedom, making the simulation impossible.

In [72], we coped with this problem by using the Adaptive Mesh Refinement option of COMSOL 5.3. Namely, we started the simulation with a rather rough homogeneous mesh. The program estimated the value of the solution's squared gradient $(\nabla u)^2$, refined the mesh locally in the domain parts where $(\nabla u)^2$ is higher than in the other places, and restimulated it on the new mesh. Thus, we obtained the mesh which is finer inside the zone interface but rougher outside it. We proceeded with the refinement up to 250 times until we obtained the desired mesh size within the zone boundary. This typically led to $\lesssim 10^5$ degrees of freedom, making the simulation plausible. Details one finds in Appendix B of the paper [72].

However, the zone size in the point indicated by the diamond in Fig. 5 is $\tau \approx 1.2 \times 10^4$ dimensionless units. The

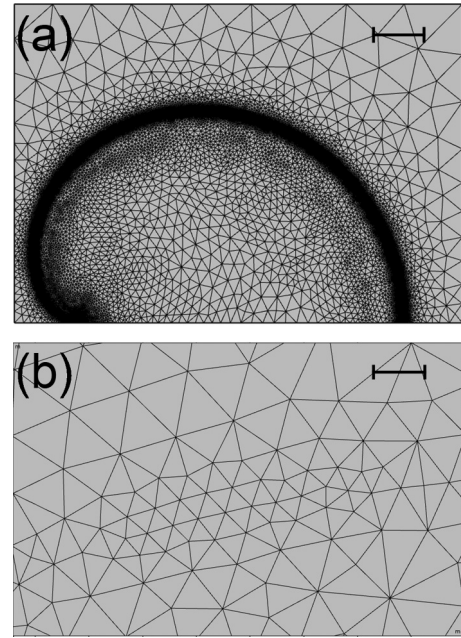


FIG. 9. Mesh obtained for the case $a = 0.20$ using the settings described in the text. (a) The mesh of the whole simulation domain. It exhibits a rough mesh far from the kink, the mesh density dramatically increasing in the kink region. The bar corresponds to 1000 dimensionless units. (b) A blown-up fragment of the same mesh from the middle of the kink. The bar shows five dimensionless units.

methods available to COMSOL 5.3 were not enough to make the solution good for numerical integration.

COMSOL 5.5 introduced a useful feature. It makes possible in time-dependent problems both the mesh refinement in the regions where $(\nabla u)^2$ is high accompanied by its roughening where $(\nabla u)^2$ is low. To achieve this, in the Adaptive Mesh Refinement Settings page, we selected the General modification as the Adaptation method, checked the Allow coarsening checkbox, and defined both the Maximum number of refinements as well as Maximum coarsening factor to be 10. The latter considerably decreased the number of degrees of freedom, enabling us to solve the problem in case $a = 0.20$ and 0.21. The mesh obtained using these settings for $a = 0.20$ is shown in Fig. 9(a).

It exhibits a rough mesh far from the kink. Close to the domain boundary, where the order parameter is close to zero, the mesh size is about 1000 dimensionless units. The mesh gradually becomes dense close to the kink, and inside the kink region the mesh size is about 1 unit [Fig. 9(b)].

The other settings were the same as reported in the paper [72].

2. Numerical calculation of the integrals

a. Estimates of the integrals of the Green function approach

We simulated Eq. (31) using COMSOL 5.5, which enables us to determine the derivatives $\partial u^2 / \partial x$ and $\partial u^2 / \partial y$ as a post-process starting from the simulation results $u = u(x, y)$.

Figure 10 shows the lateral behavior of these derivatives in the case $a = 0.24$. For each distribution we chose a perspective enabling one to best see its details. We obtained the analogous distributions for all of the other a values, which

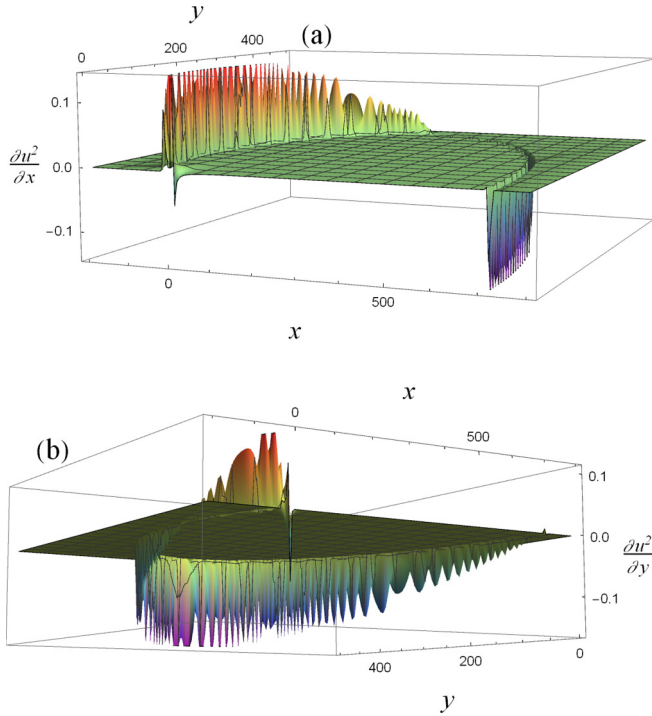


FIG. 10. The lateral behavior of $\partial u^2/\partial x$ (a) and $\partial u^2/\partial y$ (b) at $a = 0.24$ and $b = 1$.

have the same forms differing from one another by their sizes. The derivatives exhibit the configurations of sharp crests localized along the zone boundary. One part of each crest lies in the upper, and the other part is situated in the lower semispaces. A portion of each distribution is, thus, positive, while the rest is negative. The detailed inspection of the distribution on a small scale shows that across the zone boundary the distribution is bell shaped, as we have shown in Fig. 12 of our previous paper [72]. A sawtooth appearance of the distribution is related to the errors introduced during the numerical determination of the derivatives $\partial u^2/\partial x$ and $\partial u^2/\partial y$ on the mesh of the data for u .

We imported the data for $\partial u^2/\partial x$ and $\partial u^2/\partial y$ into MATHEMATICA 12.1 and interpolated them. Furthermore, we calculated the integral (47) at $\nu = 1/3$. In this case, the functions $P_1(\xi, x, y)$ and $P_2(\xi, x, y)$ (48, 49) take the following forms:

$$P_1(\xi, x, y) = -\frac{(x + \xi)[5y^2 - (x + \xi)^2]}{(2\pi)^{3/2}[(x + \xi)^2 + y^2]^2},$$

$$P_2(\xi, x, y) = -\frac{y[7y^2 + (x + \xi)^2]}{(2\pi)^{3/2}[(x + \xi)^2 + y^2]^2}. \quad (\text{A2})$$

With the obtained interpolation functions for $\partial u^2/\partial x$ and $\partial u^2/\partial y$ as well as with $P_1(\xi, x, y)$ and $P_2(\xi, x, y)$ (A2), we numerically estimated the integral (47) using the built-in numerical routine NIntegrate of MATHEMATICA 12.1. The integral exists; however, because the functions $P_1(\xi, x, y)$ and $P_2(\xi, x, y)$ are singular at $x = -\xi$ and $y = 0$, one needs to use a specific strategy yielding the numeric convergence. We selected the strategy with sampling the points according to the 3D Cartesian rule, and applied the Gauss-

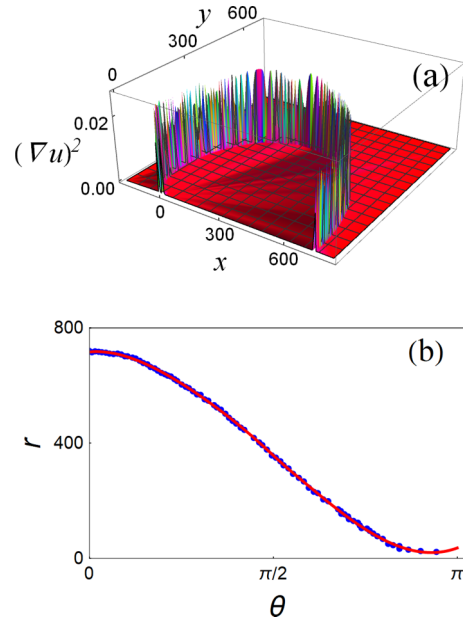


FIG. 11. (a) The lateral distribution of $(\nabla u)^2$ for $a = 0.24$. (b) The coordinates of the points of its crest transformed to cylindrical coordinates $r = r(\theta)$. The dots indicate the boundary points obtained from the simulation data, while the solid line shows its fitting.

Kronrod approach with additional Gauss points. The options used are Points $\rightarrow 3$, MinRecursion $\rightarrow 3$, MaxRecursion $\rightarrow 7$, Exclusions $\rightarrow \{0, 0, 0\}$. In the integral with respect to ξ , we took a finite upper limit equal to the coordinate x of the left boundary of the domain Ω instead of infinity. This does not influence the result, because at this value of ξ the derivatives $\partial u^2/\partial x$ and $\partial u^2/\partial y$ are practically zero. With these parameters, we achieved the error within a few percent and a reasonable calculation time below 10 min, depending on the size of the integration domain.

b. Integration within the approach using the weight functions

On the basis of the COMSOL simulation we obtained the distribution of $(\nabla u)^2 = (\partial u/\partial x)^2 + (\partial u/\partial y)^2$ and imported it into MATHEMATICA 12.1. This distribution always represents a sharp crest along the zone boundary with a bell-shaped cross section. $(\nabla u)^2$ is always positive. Figure 11(a) displays the example of such a distribution for $a = 0.24$. The $(\nabla u)^2$ distributions at other a values have qualitatively the same configurations and only differ from one another by their sizes.

As in the previous case, the sawtooth shape is due to errors introduced by numerical differentiation. The height of the crest points varies along the zone contour. In the list yielding this distribution, we selected points lying in the close vicinity of the crest in the Cartesian coordinates by requiring $(\nabla u)^2$ to be greater than a certain value. The latter was chosen by trial and error in the range from 0.005 to 0.02. These points accurately represent the zone boundary contour. Examples of the zone contour obtained by such a procedure are shown in Figs. 4(b) and 4(c). We transformed these lists to show the points of the boundaries in the cylindrical coordinates $r = r(\theta)$ [shown by dots in Fig. 11(b)].

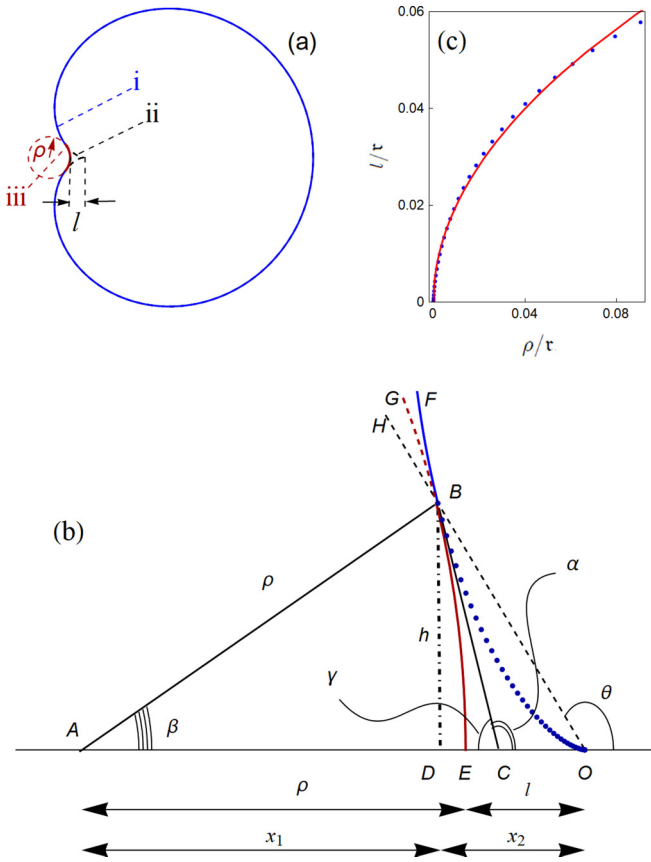


FIG. 12. (a) The cardioid contour (i), its cusp (ii), and the continuous, smooth continuation of the cardioid contour by the circular arc (iii). The curvature radius ρ and the setback l are indicated. (b) The blown-up fragment of the image shown in (a) with the geometrical notations used in the derivation below. (c) Dependence of l/τ on ρ/τ . The dots are obtained with (B4) while the solid line shows it fitting with Eq. (B5).

We further divided the interval $0 \leq \theta \leq \pi$ into three overlapping intervals: $0 \leq \theta \leq \theta_1 + 0.1$, $\theta_1 - 0.1 \leq \theta \leq \theta_2 + 0.1$, and $\theta_2 - 0.1 \leq \theta \leq \pi$. Within each interval, we fitted the curves by a fourth-order polynomial in terms of the angle θ using the standard FindFit routine of MATHEMATICA. By trial and error, we varied the boundaries θ_1 and θ_2 of the intervals, which allowed us to achieve continuous and piecewise smooth curves. Given that we then used the fitting functions for the integration, the existence of two kink points introduces a negligible error to the result. The fitting result is shown by the solid line in Fig. 11(b). We obtained analogous results for all a values.

We substituted the obtained analytical functions fitting $r(\theta)$ into the integral I (59) and numerically estimated the integral using the standard NIntegrate routine of MATHEMATICA 12.1. In this case, the integration was straightforward.

APPENDIX B: THE SETBACK

Our simulations [72] demonstrate that for the motionless crack, most of the zone boundary closely resembles the cardioid, as shown in Fig. 12(a) i. Here the boundary curvature radius R_c is of the same order of magnitude as the zone

width τ . Because $\tau \gg 1$, the boundary surface tension almost everywhere plays a negligible role.

The situation is different in the vicinity of the beak-shaped part of the cardioid shown in Fig. 12(a) ii. Due to its surface tension, this configuration of the boundary is energetically unfavorable. Instead, the backward zone part forms an invagination with the bottom in the form of an arc of a circle, as we show schematically in Fig. 12(a) iii. The derivation of the exact expression for its curvature radius ρ we reported in [82]. The expression for ρ takes the following form:

$$\rho = \frac{\sqrt{6|b^2 - 2a + b\sqrt{b^2 - 4a}|^{1/2}}}{8a - b^2 - b\sqrt{b^2 - 4a}}. \quad (\text{B1})$$

It is this mechanism that forms the setback observed in our simulations.

Let us derive the analytical approximation for the contact length l [also indicated in Fig. 12(a)]. We approximate the boundary invagination by a portion of the circle with the radius ρ . This circular arc must pass into the cardioid contour continuously and smoothly [Fig. 12(a) iii].

Figure 12(b) shows the blown-up part of the image Fig. 12(a) in the vicinity of the cusp with a detailed view of the circular arc EBG inscribed into the cardioid OBF such that the zone contour is continuous-smooth. The sketch indicates the sizes in terms of the dimensionless units that we introduced earlier. The zone interface consists of the circular arc EB [Fig. 12(a) iii] followed by the portion of the cardioid BF [Fig. 12(a) i]. Both parts of the interface are shown by the solid lines. The dashed line BG is the continuation of the circle, while the dotted one, OB, is the continuation of the cardioid from the point B to the coordinate origin O corresponding to Fig. 12(a) ii. They do not correspond to the zone boundary.

The arc GBE touches the contour OBF of the cardioid in the point B, where they have a common tangent BC. The latter has a slope angle α . The distance between the cardioid origin O and the point E, where the circular arc hits the x axis, is the contact length, l . The angle subtended at A by B is β , and that at O by B is θ . Furthermore, h is the height BD (dotted line) of the triangle ABC. AB and AE are equal to the arc curvature radius ρ . Let us denote AD as x_1 , while DO is denoted as x_2 . The cardioid can be parametrically described as

$$\mathbf{r}(\theta) = \tau \cos^2(\theta/2)(\cos \theta, \sin \theta) \quad (\text{B2})$$

where τ is the dimensionless zone width. By using (B2) one finds the slope, $\tan(\alpha)$, of the tangent BC as follows: $\tan(\alpha) = -\cot(3\theta/2)$. Let us introduce the angle $\varphi = \pi - \alpha$. One finds $\beta = (\pi - 3\varphi)/2$.

From the triangle, ABC $h = \rho \sin(\beta) = \rho \cos(3\varphi/2)$. Meanwhile, h is equal to the Y coordinate in point B. In terms of the angle φ one finds $h = \tau \sin^2(\varphi/2) \sin(\varphi)$. Equating the two latter expressions for h one derives the following equation:

$$\frac{\rho}{\tau} = \frac{\sin^2(\varphi/2) \sin(\varphi)}{\cos(3\varphi/2)}. \quad (\text{B3})$$

Let us determine the values x_1 , x_2 , and l . It is easy to see that $x_1 = \rho \cos(\beta) = \rho \sin(3\varphi/2)$. One finds the value of x_2 as the projection of the cardioid point, B, onto the X

axis yielding $x_2 = \tau \sin^2(\varphi/2) \cos(\varphi)$. Finally, the dimensionless contact length expresses as $l = x_1 + x_2 - \rho$. It follows that $l/\tau = (\rho/\tau)[\sin(3\varphi/2) - 1] + \cos(\varphi) \sin^2(\varphi/2)$. By substituting here the expression for ρ/τ Eq. (B3) we obtain

$$\frac{l}{\tau} = \frac{\sin^2(\varphi/2)}{1 + 2 \sin(\varphi/2)}. \quad (\text{B4})$$

Together, Eqs. (B3) and (B4) determine the dependence l/τ on ρ/τ in the parametric form.

During our simulations we observed that the inequality $\rho/\tau < 0.1$ typically holds. Therefore, we only regard this case. The dependence l/τ on ρ/τ , according to Eqs. (B3) and (B4), we display by dots in Fig. 12(c). At $\rho/\tau < 0.1$ one can accurately fit these points by the following relation:

$$l \approx 0.2(\rho \tau)^{1/2}. \quad (\text{B5})$$

The fitting by (B5) is shown by the solid line in Fig. 12(c). One expresses the dimensionless zone size τ at the tip of the motionless crack using (38). By combining (B5) and (B1) one finds the analytical expression for the dimensional contact length expressed by the relation (39) with $l_0 \approx 6.69$.

Let us note that due to the surface tension, the concave meniscus [Fig. 12(a) iii] deforms the zone at its back, exerting a configurational force on the boundary. The latter is directed against the x axis. In the present derivation, we disregarded its effect. Thus, this result underestimates the correct value of the contact length. Indeed, the curve (39) with $l_0 \approx 6.69$ lies systematically slightly below the values obtained by simulations and shown by dots. We corrected it by fitting the numerical parameter l_0 to the points taken from the simulations yielding $l_0 \approx 10.42$. The run of this curve is shown by the solid line in Fig. 5(b).

-
- [1] S. K. Hann and J. D. Gates, *J. Mater. Sci.* **32**, 1249 (1997); Z. Khan and M. Ahmed, *J. Mater. Eng. Perform.* **5**, 201 (1996); M. K. Banerjee, N. R. Bandyopadhyay, and J. Mazumder, *Processing and Fabrication of Advanced Materials VI* (IOM Communications, London, 1998), Vols. 1 and 2.
- [2] S. D. Antolovich, *Trans. Metall. Soc. AIME* **242**, 2371 (1968); S. D. Antolovich and D. Fahr, *Eng. Fract. Mech.* **4**, 133 (1972).
- [3] E. C. Oliver, P. J. Withers, M. R. Daymond, S. Ueta, and T. Mori, *Appl. Phys.* **74**, S1143 (2002); S. Papaefthymiou, W. Bleck, U. Prah, C. Acht, J. Sietsma, and S. van der Zwaag, in *Materials Science Forum*, Vol. 426–432, (Trans Tech Publications, Ltd., 2003), pp. 1355–1360; H. Oettel and U. Martin, *Int. J. Mat. Res.* **97**, 1642 (2006); H. Oettel, M. Glavatskikh, U. Martin, and A. Nikulin, in *Materials Science Forum*, Vol. 539–543, (Trans Tech Publications, Ltd., 2007), pp. 4903–4908; M. Zhang, L. Li, Y. Su, R. Fu, Z. Wan, and B. C. de Cooman, *Steel Research Int.* **78**, 501 (2007).
- [4] L. E. Tanner, D. Schryvers, and S. M. Shapiro, *Mater. Sci. Eng.* **A127**, 205 (1990); K. Kimura, T. Asaoka, and K. Funami, in *THERMEC'97, Vols I-II*, edited by T. Chandra and T. Sakai (Minerals, Metals and Materials Society, Warrendale, PA, USA, 1997), p. 1675; U. D. Hangen and G. Sauthoff, *Intermetallics* **7**, 501 (1999); H. F. Lopez, *Mater. Lett.* **51**, 144 (2001); G. M. Loughran, T. W. Shield, and P. H. Leo, *Int. J. Solids Struct.* **40**, 271 (2003); F. Xiong and Y. Liu, *Acta Mater.* **55**, 5621 (2007); S. Gollerthan, M. L. Young, K. Neuking, U. Ramamurty, and G. Eggeler, *ibid.* **57**, 5892 (2009); H. Qiu, L. N. Wang, J. G. Qi, H. Zuo, and K. Hiraoka, *Mater. Sci. Eng.* **A579**, 71 (2013).
- [5] J. A. Horton, J. L. Wright, and J. H. Schneibel, in *Bulk Metallic Glasses*, edited by W. L. Johnson, A. Inoue, and C. T. Liu (Cambridge University, Cambridge, England, 1999), Vol. 554, p. 185.
- [6] T. Sasaki, N. Shibata, K. Matsunaga, T. Yamamoto, and Y. Ikuhara, *J. Ceram. Soc. Jpn.* **120**, 473 (2012).
- [7] L. Zhao, D. Bardel, A. Maynadier, and D. Nelias, *Scr. Mater.* **130**, 83 (2017).
- [8] S. O. Kramarov, N. Y. Egorov, and L. M. Katsnel'son, *Fiz. Tverd. Tela* **28**, 2858 (1986) [*Sov. Phys. Solid State* **28**, 1602 (1986)].
- [9] Y.-H. Seo, J. Koruza, A. Benčan, B. Malič, J. Rödel, K. G. Webber, and C. Landis, *J. Am. Ceram. Soc.* **97**, 1582 (2014).
- [10] C. S. Lynch, R. M. McMeeking, and Z. Suo, in *Second International Conference on Intelligent Materials ICIM '94*, edited by C. A. Rogers and G. G. Wallace (Technomic, Lancaster, PA, 1994), p. 856.
- [11] R. C. Garvi Hannink, and R. T. Pascoe, *Nature (London)* **258**, 703 (1975); L. K. Lenz and A. H. Heuer, *J. Am. Ceram. Soc.* **65**, C-192 (1982); R. P. Indel, R. W. Rice, and D. Lewis, *ibid.* **65**, c108 (1982); F. F. Lange, *J. Mater. Sci.* **17**, 240 (1982).
- [12] D. L. Porter and A. H. Heuer, *J. Am. Ceram. Soc.* **60**, 183 (1977).
- [13] P. M. Kelly and L. R. F. Rose, *Progr. Mater. Sci.* **47**, 463 (2002).
- [14] M. T. Dorn and K. G. Nickel, in *High-Pressure Surface Science and Engineering*, edited by Y. Gogotsi and V. Domnich (Institute of Physics, Bristol, 2004), pp. 467–520; B. Basu, *Int. Mater. Rev.* **50**, 239 (2005); G. A. Gogotsi *et al.*, *Ceram. Int.* **36**, 345 (2010).
- [15] A. Apte *et al.*, *Acs Nano* **12**, 3468 (2018).
- [16] H.-J. Sue, J. D. Earls, and R. E. Hefner, Jr., *J. Mater. Sci.* **32**, 4039 (1997).
- [17] J. Karger-Kocsis and J. Varga, *J. Appl. Polym. Sci.* **62**, 291 (1996); S. T. Kim, J. Kim, S. Lim, C. R. Choe, and S. I. Hong, *J. Mater. Sci.* **33**, 2421 (1998); G. A. Maier, G. Wallner, R. W. Lang, and P. Fratzl, *Macromolecules* **38**, 6099 (2005); T. Koyama, T. Araki, and H. Tanaka, *Phys. Rev. Lett.* **102**, 065701 (2009); J. A. Donovan, *Nippon Gomu Kyokaishi* **75**, 239 (2002); S. Trabelsi, P.-A. Albouy, and J. Rault, *Macromolecules* **35**, 10054 (2002); H. P. Zhang, J. Niemczura, G. Dennis, K. Ravi-Chandar, and M. Marder, *Phys. Rev. Lett.* **102**, 245503 (2009); J. R. S. Martinez, X. Balandraud, E. Toussaint, J. B. Le Cam, and D. Berghezan, *Polymer* **55**, 6345 (2014).
- [18] H. Toda, *Microscopy* **63**, i3.1 (2014).
- [19] S. J. Pennycook, *Ultramicroscopy* **123**, 28 (2012).
- [20] S. J. Wang, H. Wang, K. Du, W. Zhang, M. L. Sui, and S. X. Mao, *Nature Com.* **5**, 3433 (2014).
- [21] L. R. F. Rose, *Proc. R. Soc. A* **412**, 169 (1987).
- [22] I. Roth, U. Krupp, H. J. Christ, M. Kuebbeler, and C. P. Fritzen, in *ESOMAT 2009—8th European Symposium on*

- Martensitic Transformations*, edited by P. Sittner, V. Paidar, and H. Seiner (EDP Sciences, Les Ulis, France, 2009), pp. 06030/1–5.
- [23] S. W. Robertson, A. Mehta, A. R. Pelton, and R. O. Ritchie, *Acta Mater.* **55**, 6198 (2007).
- [24] F. Meschke, O. Raddatz, A. Kolleck, and G. A. Schneider, *J. Am. Ceram. Soc.* **83**, 353 (2000).
- [25] Y. H. Lu, S. Liang, W. Y. Chu, and L. J. Qiao, *Intermetallics* **10**, 823 (2002).
- [26] K. Yoshida, F. Wakai, N. Nishiyama, R. Sekine, Y. Shinoda, T. Akatsu, T. Nagoshi, and M. Sone, *Sci. Rep.* **5**, 10993 (2015).
- [27] T. K. Gupta, in *Fracture Mechanics of Ceramics*, edited by R. C. Bradt (Plenum, New York, 1978), pp. 877–889.
- [28] T. K. Gupta, F. F. Lange, and J. H. Behtold, *J. Mater. Sci.* **13**, 1464 (1978).
- [29] N. Claussen, *Z. Werkstofftechnik* **13**, 138 (1982).
- [30] P. F. Becher and V. J. Tennery, in *Fracture Mechanics of Ceramics*, edited by R. C. Bradt (Plenum, New York, 1983), Vol. 6, p. 383.
- [31] K. Tsukuma and M. Shimada, *J. Mater. Sci.* **20**, 1178 (1985); A. G. Evance, *J. Am. Ceram. Soc.* **73**, 187 (1990).
- [32] K. Nishimura and N. Miyazaki, *Comput. Model. Eng. Sci.* **2**, 143 (2001); A. Latapie and D. Farkas, *Model. Simul. Mater. Sci. Eng.* **11**, 745 (2003); R. Matsumoto, M. Nakagaki, A. Nakatani, and H. Kitagawa, *Comput. Model. Eng. Sci.* **9**, 75 (2005); Y.-F. Guo, Y.-S. Wang, and D.-L. Zhao, *Acta Mater.* **55**, 401 (2007); V. A. Borodin and P. V. Vladimirov, *J. Nuclear Mater.* **415**, 320 (2011).
- [33] R. Matsumoto, M. Nakagaki, A. Nakatani, and H. Kitagawa, *Cmes-Computer Model. Eng. Sci.* **9**, 75 (2005).
- [34] M. J. Buehler, H. Tang, A. C. T. van Duin, and W. A. Goddard, *Phys. Rev. Lett.* **99**, 165502 (2007); D. Sherman, M. Markovitz, and O. Barkai, *J. Mech. Phys. Solids* **56**, 376 (2008); F. Atrash and D. Sherman, *ibid.* **60**, 844 (2012).
- [35] J. R. Kermode, T. Albaret, D. Sherman, N. Bernstein, P. Gumbsch, M. C. Payne, G. Csanyi, and A. De Vita, *Nature (London)* **455**, 1224 (2008).
- [36] J. Mei, Y. Ni, and J. Li, *Int. J. Solids Struct.* **48**, 3054 (2011).
- [37] M. Ruda, D. Farkas, and G. Bertolino, *Comput. Mater. Sci.* **49**, 743 (2010).
- [38] C. Wang, R. Feng, D. J. Diestler, and X. C. Zeng, *J. Appl. Phys.* **108**, 013527 (2010).
- [39] Y. Zhang, X.-Y. Liu, P. C. Millett, M. Tonks, D. A. Andersson, and B. Biner, *J. Nucl. Mater.* **430**, 96 (2012).
- [40] Y.-F. Guo, Y.-S. Wang, W.-P. Wu, and D.-L. Zhao, *Acta Mater.* **55**, 3891 (2007).
- [41] A. Falvo, F. Furgiuele, A. Leonardi, and C. Maletta, *J. Mater. Eng. Perform.* **18**, 679 (2009).
- [42] F. F. Abraham, D. Brodbeck, R. A. Rafey, and W. E. Rudge, *Phys. Rev. Lett.* **73**, 272 (1994); S. J. Zhou, P. S. Lomdahl, R. Thomson, and B. L. Holian, *ibid.* **76**, 2318 (1996); P. Gumbsch, S. J. Zhou, and B. L. Holian, *Phys. Rev. B* **55**, 3445 (1997); T. Cramer, A. Wanner, and P. Gumbsch, *Phys. Rev. Lett.* **85**, 788 (2000).
- [43] Y.-F. Guo and D.-L. Zhao, *Mater. Sci. Eng.* **A448**, 281 (2007).
- [44] I. Birkby and R. Stevens, *Key Eng. Mater.* **122–124**, 527 (1996).
- [45] R. I. Todd and M. P. S. Saran, Transformation toughening, in *Materials Processing Handbook*, edited by J. R. Groza (CRC, Boca Raton, FL, 2007), Vol. 20, pp. 1–20.
- [46] B. L. Karihaloo and J. H. Andreasen, *Mechanics of Transformation Toughening and Related Topics* (Elsevier, Amsterdam, 1996).
- [47] A. G. Evans and R. M. Cannon, *Acta Metall.* **34**, 761 (1986).
- [48] R. M. McMeeking and A. G. Evans, *J. Am. Ceram. Soc.* **65**, 242 (1982).
- [49] B. Budiansky, J. W. Hutchinson, and J. C. Lambropoulos, *Int. J. Solids Struct.* **19**, 337 (1983).
- [50] L. R. F. Rose, *J. Mech. Phys. Solids* **19**, 337 (1986).
- [51] J. W. Hutchinson, Harvard University Report No. DEAP S-8, Division of Applied Science, 1974.
- [52] D. M. Stump and B. Budiansky, *Acta Metall.* **37**, 3297 (1989).
- [53] D. M. Stump, *Philos. Mag. A* **64**, 879 (1991).
- [54] G. T. M. Stam, E. v. d. Giessen, and P. Meijers, *Int. J. Solids Structures* **31**, 1923 (1994).
- [55] B. Budiansky and L. Truskinovsky, *J. Mech. Phys. Solids* **41**, 1445 (1993).
- [56] N. Simha and L. Truskinovsky, *Acta Metall. Mater.* **42**, 3827 (1994).
- [57] Y. Freed and L. Banks-Sills, *J. Mech. Phys. Solids* **55**, 2157 (2007).
- [58] T. Baxevanis, Y. Chemisky, and D. C. Lagoudas, *Smart Mater. Structures* **21**, 094012 (2012).
- [59] T. Baxevanis, A. F. Parrinello, and D. C. Lagoudas, *Int. J. Plasticity* **50**, 158 (2013).
- [60] L. Ma, A. M. Korsunsky, and R. M. McMeeking, *J. Appl. Mech. Trans. ASME* **80**, 051001 (2013).
- [61] C. LExcellent and F. Thiebaud, *Scr. Mater.* **59**, 321 (2008); C. LExcellent, M. R. Laydi, and V. Tallebot, *Int. J. Fracture* **169**, 1 (2011).
- [62] C. Maletta and F. Furgiuele, *Acta Mater* **58**, 92 (2010); C. Maletta, E. Sgambitterra, and F. Furgiuele, *Fatigue Fract. Eng. Mater. Structures* **36**, 903 (2013); S. Hazar, W. Zaki, Z. Moumni, and G. Anlas, *Int. J. Plasticity* **67**, 26 (2015).
- [63] C. Maletta and M. L. Young, *J. Mater. Eng. Performance* **20**, 597 (2011).
- [64] U. Krupp, I. Roth, H. J. Christ, M. Kübbeler, C. P. Fritzen, M. Scharnweber, C.G. Oertel, and W. Skrotzki, in *Materials Structure and Micromechanics of Fracture*, edited by P. Sandera (Trans Tech Publications, Durnten-Zurich, Switzerland, 2011), Vol. 465, p. 55.
- [65] I. R. Vatne, A. Stukowski, C. Thaulow, E. Ostby, and J. Marian, *Mater. Sci. Eng.* **A560**, 306 (2013).
- [66] J. Corteen, M. Rainforth, and I. Todd, *Scr. Mater.* **65**, 524 (2011).
- [67] K. Kim, J. Geringer, and B. Forest, *Eng. Comput.* **30**, 648 (2013); D. Gastaldi, *Int. J. Mater. Product Technol.* **35**, 346 (2009).
- [68] A. A. Bulbich, *J. Mater. Sci.* **27**, 1070 (1992).
- [69] L. Ma, *Int. J. Solids Structures* **47**, 3214 (2010).
- [70] A. L. Roitburd, *Sov. Phys. Usp.* **17**, 326 (1974); *Sov. Phys. Solid State* **26**, 1229 (1984); M. A. Grinfel'd, *Lett. Appl. Eng. Sci.* **19**, 1031 (1981); *Izvestia, Earth Phys.* **18**, 28 (1982).
- [71] A. Boulbitch and A. L. Korzhenevskii, *Phys. Rev. B* **96**, 054106 (2017).
- [72] A. Boulbitch and A. L. Korzhenevskii, *Phys. Rev. E* **101**, 033003 (2020).
- [73] J. C. Burfoot and T. J. Parker, *Brit. J. Appl. Phys.* **17**, 213 (1966); T. Nakamura and H. Ihara, *J. Phys. Soc. Jpn. Suppl.* (1970) **28**, 204 (1969); J. Dec, *J. Phys. C* **21**, 1257 (1988);

- Ferroelectrics* **89**, 193 (1989); V. S. Boyko, R. I. Garber, and A. M. Kosevich, *Reversible Crystal Plasticity* (Springer-Verlag, Berlin, 1994); S. M. Yufatova, Y. G. Sindeyev, V. G. Gavrilyachenko, and E. G. Fesenko, *ibid.* **26**, 809 (1980); R. Vlokh, H. Kabelka, H. Warhanek, I. Skab, and O. V. Vlokh, *Phys. Status Solidi A* **168**, 397 (1998); A. Yangui, M. Sy, L. Li, Y. Abid, P. Naumov, and K. Boukheddaden, *Sci. Rep.* **5**, 16634 (2015); J. Yoon, H. Kim, X. Chen, N. Tamura, B. S. Mun, C. Park, and H. Ju, *ACS Appl. Mater. Interfaces* **8**, 2280 (2016); G. Zijlstra, M. S. B. van Daalen, D. I. Vainchtein, V. Ocelik, and J. T. M. de Hosson, *Mater. Des.* **132**, 138 (2017).
- [74] L. D. Landau and E. M. Lifshitz, *Statistical Physics*, 3rd ed. (Pergamon, Oxford, 1985).
- [75] V. M. Nabutovsky and B. Y. Shapiro, *ZhETF* **75**, 948 (1978); *Sov. Phys. JETP* **48**, 480 (1978).
- [76] A. A. Boulbitch and P. Toledano, *Phys. Rev. Lett.* **81**, 838 (1998).
- [77] A. Boulbitch and A. L. Korzhenevskii, *Eur. J. Phys.* **B89**, 261 (2016).
- [78] A. Boulbitch, Y. M. Gufan, and A. L. Korzhenevskii, *Phys. Rev. E* **96**, 013005 (2017).
- [79] A. Boulbitch and A. L. Korzhenevskii, *Phys. Rev. Lett.* **107**, 085505 (2011).
- [80] A. Boulbitch and A. L. Korzhenevskii, *Phys. Rev. E* **93**, 063001 (2016).
- [81] A. Boulbitch and A. L. Korzhenevskii, *Europhys. Lett.* **123**, 16003 (2018).
- [82] A. Boulbitch and A. L. Korzhenevskii, *Phys. Rev. E* **101**, 033004 (2020).
- [83] C. F. Nigro, C. Bjerken, and P. A. Olsson, *Int. J. Fract.* **209**, 91 (2017).
- [84] T. Sluka, K. G. Webber, E. Colla, and D. Damjanovic, *Acta Mater.* **60**, 5172 (2012); H. Yu, J. Wang, S. Kozinov, and M. Kuna, *ibid.* **154**, 334 (2018).
- [85] M. Mamivand, M. A. Zaeem, and H. E. Kadiri, *Acta Mater.* **64**, 208 (2014).
- [86] T. Zhao, J. Zhu, and J. Luo, *Eng. Fracture Mech.* **159**, 155 (2016).
- [87] J. Zhu and J. Luo, *Mater. Sci. Eng A* **701**, 69 (2017).
- [88] H. Jafarzadeh, V. I. Levitas, G. H. Farrahi, and M. Javanbakht, *Nanoscale* **11**, 22243 (2019).
- [89] V. I. Levitas, H. Jafarzadeh, G. H. Farrahi, and M. Javanbakht, *Int. J. Plasticity* **111**, 1 (2018).
- [90] J. C. Toledano and P. Toledano, *The Landau Theory of Phase Transitions* (World Scientific, Singapore, 1987).
- [91] M. Mamivand, M. A. Zaeem, and H. E. Kadiri, *Comput. Mater. Sci.* **77**, 304 (2013).
- [92] Y. M. Gufan, *Structural Phase Transitions* (Nauka, Moscow, 1983) [in Russian].
- [93] A. D. Bruce and R. A. Cowley, *Structural Phase Transitions* (Taylor & Francis, London, 1981).
- [94] V. P. Sakhnenko and V. M. Talanov, *Sov. Phys. Solid State* **21**, 1401 (1979); **22**, 458 (1980).
- [95] E. Bouchbinder, A. Livne, and J. Fineberg, *Phys. Rev. Lett.* **101**, 264302 (2008); A. Livne, E. Bouchbinder, and J. Fineberg, *ibid.* **101**, 264301 (2008).
- [96] S. P. Zolotarev, I. V. Sidorova, Y. A. Skakov, and V. A. Solovev, *Sov. Phys. Solid State* **20**, 450 (1978); M. V. Belousov and B. E. Volf, *JETP Lett.* **31**, 317 (1980); N. Osakabe, K. Yagi, and G. Honjo, *Jap. J. Appl. Phys.* **19**, L309 (1980); V. K. Vlasko-Vlasov, L. M. Dedukh, and V. I. Nikitenko, *Sov. Phys. Solid State* **23**, 1085 (1981); V. K. Vlasko-Vlasov and M. V. Indenbom, *Sov. Phys. JETP* **59**, 633 (1984); A. L. Korzhenevskii, *Sov. Phys. Solid State* **28**, 1999 (1986); I. Drevensek, M. Zgonik, M. Copic, R. Blinc, A. Fuith, W. Schranz, M. Fally, and H. Warhanek, *Phys. Rev. B* **49**, 3082 (1994); D. B. Ge, V. Domnich, and Y. Gogotsi, *J. Appl. Phys.* **93**, 2418 (2003); A. Sohn, T. Kanki, H. Tanaka, and D. W. Kim, *Appl. Phys. Lett.* **107**, 171603 (2015); I. N. Khlyustikov and A. I. Buzdin, *Sov. Phys. Usp.* **31**, 409 (1988).
- [97] G. P. Cherepanov, *Mechanics of Brittle Fracture* (McGraw-Hill, New York, 1979); N. F. Morozov, *Mathematical Problems of the Theory of Cracks* (Nauka, Moscow, 1984) [in Russian].
- [98] H. F. Bueckner, *Trans. ASME* **80**, 1225 (1958).
- [99] N. I. Muschelisvili, *Some Basic Problems of the Mathematical Theory of Elasticity*, reprint of the second English edition, translated by J. R. M. Radok (Noordhoff, Leyden, The Netherlands, 1977).
- [100] Section 57, p. 218 of the book [99].
- [101] H. F. Bueckner, *Z. Angew. Math. Mech.* **50**, 529 (1970).
- [102] S. G. Dzhabarov, *Usp. Fiz. Met.* **16**, 329 (2015); T. Ishidate, S. Abe, H. Takahashi, and N. Mōri, *Phys. Rev. Lett.* **78**, 2397 (1997).
- [103] A. Z. Patashinskij and V. L. Pokrovskij, *Fluctuation Theory of Phase Transitions* (Pergamon, Oxford, 1979).
- [104] M. E. Lines and A. M. Glass, *Principles and Applications of Ferroelectrics and Related Materials* (Clarendon, Oxford, 1977).
- [105] A. Onuki, *Phase Transitions Dynamics* (Cambridge University, Cambridge, England, 2002).
- [106] T. A. Aslanian and A. P. Levanyuk, *Solid State Commun.* **31**, 547 (1979).
- [107] E. Y. Tonkov, *High Pressure Phase Transformations: A Handbook* (Gordon and Breach, New York, 1992), Vols. 1–3.
- [108] G. A. Schneider, *Ann. Rev. Matter. Res.* **37**, 491 (2007).
- [109] A. Mesgarnejad, A. Immanian, and A. Karma, *Theor. Appl. Fracture Mech.* **103**, 102282 (2019).
- [110] G. H. Farrachi, M. Javanbakht, and H. Jafarzadeh, *Continuum Mech. Thermodyn.* **32**, 589 (2018).
- [111] M. Zecevic, M. J. Cawkwell, K. J. Ramos, and D. J. Luscher, *Modelling Simulation Mater. Sci. Eng.* **28**, 055002 (2020).
- [112] Y. L. Wang, A. K. Tagantsev, D. Damjanovic, N. Setter, V. K. Yarmarkin, A. I. Sokolov, and I. A. Lukyancuk, *J. Appl. Phys.* **101**, 104115 (2007).
- [113] A. J. Bell and L. E. Cross, *Ferroelectrics* **59**, 197 (1984); A. J. Bell, *J. Appl. Phys.* **89**, 3907 (2001); Y. L. Li, L. E. Cross, and L. Q. Chen, *ibid.* **98**, 064101 (2005); L. Q. Chen, in *Physics of Ferroelectrics: A Modern Perspective*, edited by K. M. Rabe, C. H. Ahn, and J. M. Triscone (Springer-Verlag, Berlin, 2007), Vol. 105, pp. 363–371; X. Lu, H. Li, and W. Cao, *ibid.* **114**, 224106 (2013).
- [114] N. Nishiyama *et al.*, *Sci. Rep.* **4**, 1 (2014).
- [115] V. P. Dmitriev, S. B. Rochal, Y. M. Gufan, P. Toledano, *Phys. Rev. Lett.* **60**, 1958 (1988); P. Toledano and V. Dmitriev, *Reconstructive phase transitions*, in *Crystals and Quasicrystals* (World Scientific, Singapore, 1996); A. L. Korzhenevskii and V. P. Dmitriev, *J. Phys.: Condens. Matter* **27**, 375401 (2015).

- [116] J. D. Eshelby, *Elastic Inclusions and Inhomogeneities* (North-Holland, Amsterdam, 1961).
- [117] P. R. Cantwell, M. Tang, S. J. Dillon, J. Luo, G. S. Rohrer, and M. P. Harmer, *Acta Mater.* **62**, 1 (2014).
- [118] J. Fridel, *Dislocations* (Pergamon, Oxford, 1964); J. P. Hirth and J. Lothe, *Theory of Dislocations* (Krieger, Malabar, FL, 1991).
- [119] V. G. Garin, *Sverhtverdye Materialy* **2**, 17 (1982) [in Russian].
- [120] M. L. Lines and A. M. Glass, *Principles and Applications of Ferroelectrics and Related Materials* (Oxford University, Oxford, 2001); V. G. Vaks, *Introduction into Microscopic Theory of Ferroelectrics* (Nauka, Moscow, 1973).
- [121] T. Ungar, J. Frenzel, S. Gollerthan, G. Ribarik, L. Balogh, and G. Eggeler, *J. Mater. Res.* **32**, 4433 (2017).
- [122] L. K. Huang, W. T. Lin, B. Lin, and F. Liu, *Acta Mater.* **118**, 306 (2016).
- [123] A. Boulbitch, *Mathematica J.* **20**, 1 (2018).